Clemson University

TigerPrints

8-2022

Creep Behavior of a Ti-based Multi-Principal Element Alloy

Benjamin Elbrecht
belbrec@g.clemson.edu

Follow this and additional works at: https://tigerprints.clemson.edu/all_theses

Part of the Applied Mechanics Commons, Metallurgy Commons, Other Materials Science and Engineering Commons, and the Other Mechanical Engineering Commons

CREEP BEHAVIOR OF A TI-BASED MULTI-PRINCIPAL ELEMENT ALLOY

A Thesis Presented to the Graduate School of Clemson University

In Partial Fulfillment of the Requirements for the Degree Master of Science

Mechanical Engineering

By:

Benjamin James Elbrecht

August 2022

Accepted by:

Dr. Garrett J. Pataky: Thesis Advisor, Committee Chair

Dr. Paul F. Joseph

Dr. Enrique Martinez Saez

Abstract

The understanding of microstructural damage mechanisms is the foundation of better understanding existing materials and future material development. There are significant challenges to measuring these damage mechanisms *in-situ* as continuous observation of the state of the microstructure is difficult or impossible for many experimental setups. This thesis presents a method for measuring grain boundary sliding (GBS) and local strain concentrations *in-situ* via a Heaviside function based algorithm. GBS is the shearing of two grains along their shared grain boundary and is a common damage mechanism in creep which presents as a discontinuity that can be measured with a Heaviside function.

Multi-principal element alloys (MPEAs) have potential to be the future of alloy design as there are limitless compositions possible which could exceed the capabilities of conventional alloys. MPEAs are a new class of alloys with a loose definition that they are made of multiple principal elements, generally with ≥5 at% of each principal element. $Ti_{80}(AlCrNb)_{20}$ is the alloy used in this thesis due to its potential as a lightweight MPEA (LMPEA) and its solid solution β titanium phase composition which is well suited for strong creep resistance. High resolution digital image correlation (HRDIC) enabled creep tests are performed to measure the GBS and other localized slip of $Ti_{80}(AlCrNb)_{20}$.

The GBS analysis code developed in this thesis utilizes the HRDIC creep data captured via optical microscope to measure GBS. Microstructural maps from electron backscatter diffraction (EBSD) are aligned with HRDIC creep imaging using fiducial markers to identify grain boundary locations, and the discontinuity across the grain boundary due to GBS was measured via a Heaviside function based algorithm. Measurement of GBS *in-situ* using an optical microscope is an advancement over existing methods by providing continuous data. This method also requires significantly less scanning electron microscope (SEM) time and access as the only SEM usage is an initial EBSD scan to identify the microstructure. Current methods utilize multiple or continuous SEM scans that can require the creep test

to be stopped temporarily. As creep testing is typically at elevated temperatures, this induces thermic cycling in the sample which prevents a pure creep test. Being able to run a pure creep test without thermic cycling or interruptions while taking continuous measurements will improve the data analysis capabilities and informativity of future testing on microstructure damage.

Acknowledgements

I would like to first thank Dr. Garrett Pataky for being my advisor for the past 2 years. His exceptionally high expectations for my work helped to keep me motivated through every experiment and rough draft. I have learned more in this field of research than I thought possible under his guidance, and I want to learn so much more.

I would like to thank Dr. Enrique Martinez Saez and Dr. Paul Joseph for agreeing to be on my committee. Their assistance is greatly appreciated to help me produce the best thesis possible. A special thank you to Dr. Enrique Martinez Saez for the many hours of computational help.

I would like to thank my family for the love and the incredible support they have provided over the years. They inspired me to learn, pursue my interests, and become the man I am today. Their endless support never goes unnoticed, and I always know that if I need help, I can always count on them.

I would like to thank my research group compatriots: Jacob Biddlecom, Kaitlynn Conway, Muhammed Kose, and Lucas Morand for the friendship we shared as office mates. You all have made a positive difference in my day-to-day life at Clemson University and helped to keep me enjoying the daily grind.

Lastly, I would like to thank all the friends and connections I have made during my time at Clemson University. It is not just the place that is special, the people there make all the difference in the world. Clemson has been my home for 7 years now, and I would not have had it any other way.

Table of Contents

List of Figures

List of Figures (Continued)

List of Figures (Continued)

List of Tables

Chapter 1. Motivation of Lightweight, High Strength, and Creep Resistant Alloys

Aerospace and power generation industries are consistently looking for materials that are lightweight and high strength in elevated temperature environments. Lightweighting components, while maintaining or improving strength, increases the efficiency of engines and turbines by reducing the weight of moving parts. Additionally, improving the creep resistance in components allows the engines and turbines to run at hotter temperatures and reduces the frequency of necessary component replacements. For example, weight reduction is highly impactful on aircraft fuel efficiency with a 25 lbs. reduction in aircraft weight equating to $500,000 in savings on fuel per year across an average size aircraft fleet [1]. Using the cost of aircraft fuel in 2018 of $2.20 per gallon, there is an estimated 227,272.7 gallons saved per year from a 25 lbs. weight reduction. Extrapolating to amount of fuel saved per lbs. of weight reduction gives a fuel savings of 9,091 gallons per lbs. of weight reduction across an average aircraft fleet.

One of the most common classes of alloys used to lightweight designs is titanium-based alloys. Ti-6Al-4V is the most used titanium-based alloy [2], but there are plenty of others that see usage in more specialized operating environments, such as Ti-13V-11Cr-3Al which is used in aircraft skins and springs [2]. Ti-6Al-4V is popular due to its excellent specific strength [3] compared to heavier structural alloys, such as steels, which makes Ti-6Al-4V an excellent alloy choice where the cost tradeoff is considered worthwhile for the performance increase [4]. Ti-6Al-4V is known for its dual phase $\alpha+\beta$ microstructure which prevents the alloy from having perfectly plastic behavior and increases the yield strength as the phase boundaries act as dislocation barriers [5]. This is worth noting as single phase β titanium can exhibit perfectly plastic behavior due to overly stabilizing the β phase, preventing α, α'-martensite, and α''-martensite from precipitate hardening the alloy [6]. A drawback to this is the phase boundaries, while acting as dislocation

barriers, will become sites of dislocation pileup in longer term usage cases, such as creep [5,7]. These dislocation pileups lead to cavitations forming which in turn causes crack initiation and eventual rupture [7]. To avoid this failure mechanism, titanium components that will be exposed to elevated temperatures and constant loading utilize a single phase β microstructure to prevent these dislocation pileups [5,8], which shifts the dominant creep mechanism to grain boundary sliding (GBS) [9]. Titanium based multi-principal element alloys (MPEAs) have potential in this role as phase composition manipulation via element composition are more flexible than conventional alloys. A highly stabilized β phase with enough α phase stabilization to strain harden is achievable in many different element compositions with the wide alloy design space of MPEAs [2,6,10,11].

GBS is a microstructure damage mechanism seen primarily in creep where two grains shear past each other along the grain boundary between them [12–15]. GBS can lead to voids forming at triple junctions of grains which may initiate cracks and lead to component failure in creep [16]. GBS is the dominant creep mechanism for β titanium [9]. β titanium is an alloy type commonly used in elevated temperature environments and creep, so there is value in developing new techniques and improving the existing tools for measuring the dominant damage mechanism, GBS. This thesis develops a technique to measure GBS *in-situ* via a Heaviside function based algorithm which can measure the microstructure discontinuities that appear, such as GBS, to characterize the room temperature creep behavior of $Ti_{80}(AlCrNb)_{20}$.

Chapter 2. Literature Review

2.1. MPEA Background

MPEAs are a relatively new alloy concept where the driving idea is to increase configurational entropy far beyond what conventional alloying techniques commonly achieve, with exceptions like Ni-based superalloys. This is done by having larger amounts of multiple elements, typically greater than 5% at% and at least four principal elements [11,17,18], although the definition is very loose allowing for flexibility in

the number of principal elements and the corresponding proportions of these elements in the alloy [11]. High entropy alloy (HEA) is another term used to describe this style of alloying and is commonly interchanged with MPEA as they are similar in definition. HEAs differ from MPEAs by being more focused on increasing configurational entropy beyond that of MPEAs, typically as high as is possible. HEAs often use an equiatomic mixture of the alloying elements to maximize the configuration entropy, such as the Cantor alloy [17], with at least five principal elements. The official definition of HEAs is twofold: must have at least five major elements with 5-35% at% each and a configurational entropy greater than 1.61R [19]. Both MPEAs and HEAs contrast significantly with conventional alloys which are most commonly a base element with small amounts of alloying elements added to adjust properties [18].

The primary reason MPEAs and HEAs were conceived is to increase alloy design possibilities. By allowing large quantities of multiple elements, the possible combinations of elements in alloys becomes effectively limitless [11]. For example, given 12 elements to choose from, there are 12 alloy systems possible using conventional alloying techniques with one principal element [11]. Given the same 12 elements, 220 unique MPEA systems with three principal elements can be made [11]. The side effect of using large quantities of multiple elements is the increase in configurational entropy of the alloy. This large configurational entropy originally led researchers to believe that MPEAs and HEAs were not possible as the extreme configurational entropy would prevent a solid solution microstructure from existing. The configurational entropy would cause all solid solutions to break up into intermetallic phases. Cantor *et al.* [17] disproved this with the development of the Cantor alloy, CoCrFeMnNi, as well as Yeh *et al.* [20] who tested multiple HEA systems, including CuCoNiCrAl$_x$Fe. This was a watershed moment in alloy development as the rapid increase in interest led to many more of these alloys being found and unlocking new classes of alloys, such as lightweight MPEAs (LMPEA) [21].

The benefit of increasing entropy is not immediately obvious as an increase in entropy would mean a decrease in configurational stability [17]. This would lead to MPEAs and HEAs being vulnerable to phase

transformations during usage, including stress-induced transformations, precipitation, and atomic diffusion at relatively low temperatures when compared to conventional alloys. However, the high configurational entropy theoretically prevents the alloy from ever reaching the true equilibrium state as there are significant numbers of local equilibria and metastable states present that slow down, prevent, and reverse transformations [17]. In practice, this does not always hold true as a wide range of MPEAs have been shown to have atomic diffusion, precipitation, and phase transformations that move the atomic structure away from a homogeneous, solid solution state towards an intermetallic composition [22–25].The computation complexities of fully modeling MPEA microstructure behavior have not been overcome yet, so modern MPEA development is typically a phase composition approximation via CALPHAD, or other computation tools, followed by a "build and check" on alloys with promising phase composition approximations [11,21].

2.2. Titanium Metallurgy

Titanium is a metal known for its exceptionally low density of 4.5 g/cm^3 and when alloyed, it boasts an impressive specific strength. A specific example is Ti-6Al-4V which has an excellent ratio of density to yield strength: 4.43 g/cm^3 and 825-869 MPa in an annealed state, respectively [3]. For comparison, 316L stainless steel has almost twice the density at 8.00 g/cm^3 and a much lower yield strength of 170 MPa [3]. Titanium can also be processed into a variety of shapes for different use cases with relative ease. Examples include casting stock materials such as billets and bars, powder sintering to near net shape, or additive manufacturing geometries unachievable via subtractive manufacturing with other options possible, albeit less common [3,4]. Titanium metallurgy and microstructure manipulation is an important part of understanding how to make such exceptional alloys [2,26,27]. Titanium has two primary stable phases: α and β [2,27]. The α phase has an HCP crystal structure, and the β phase has a BCC crystal structure. The elements used to change the phase stability and the processing used to manipulate the amount of each phase, grain sizes, and grain shapes are what defines the properties of titanium alloys [28,29].

The defining feature of phase stability in titanium alloys is the beta transus temperature. The beta transus temperature is the temperature above which the stable phase is the β phase, below the stable phase is the α phase [2]. The beta transus temperature is manipulated via the alloy composition as some elements will stabilize the α phase, raising the beta transus temperature, and other elements will stabilize the β phase, lowering the beta transus temperature [2]. Many titanium alloys will have a combination of both, so they have dual phase α+β microstructures. An example of this would be, again, Ti-6Al-4V [7].

The phase composition and ultimate tensile strength (UTS) of a titanium alloy can be predicted via the aluminum and molybdenum equivalencies [2,30]. Early in the development of titanium alloys, aluminum and molybdenum were the most used alloying elements, so their impact on phase stability and UTS was well documented [2,30]. As more elements were alloyed with titanium, their phase stability and UTS impact was quantified against the known effects of molybdenum and aluminum, and a summation of ratios was developed to approximate the aluminum and molybdenum equivalencies. Eqn. 1 and 2 are the aluminum and molybdenum equivalencies for UTS prediction in eqn. 3 [30].

$$Al_{eq} = wt\%Al + \frac{wt\%Sn}{2} + \frac{wt\%Zr}{3} + 3.3 * wt\%Si + 3.8 \tag{1}$$

$$Mo_{eq} = wt\%Mo + \frac{wt\%V}{1.7} + \frac{wt\%Cr}{0.8} + \frac{wt\%Fe}{0.7} + \frac{wt\%Nb}{3.3} \tag{2}$$

$$\sigma_{UTS} = 235 + 60 * Al_{eq} + 50 * Mo_{eq} \tag{3}$$

Al_{eq} and Mo_{eq} are the aluminum and molybdenum equivalency, respectively. All wt% terms are the weight percentage of total atomic weight of the respective element. σ is the UTS prediction based on aluminum and molybdenum equivalency. The aluminum equivalency defines the α phase strengthening of the alloying elements and the molybdenum equivalency defines the β phase strengthening of the alloying elements. The elements listed in Eqns. 1 and 2 have a measured strengthening effect on their respective phases, and the ratios quantify that into a scalar. For example, refractory elements like vanadium and niobium stabilize and strengthen the β phase of titanium. The UTS prediction is shown in Eqn. 3 and is

5

noted to only hold for single phase α, near α, and α+β phase compositions with a fine-grained globular structure. No specific grain size is given [30]. Predictions for near β and stable β alloys are invalid as a solid solution β titanium is noted to limit the possible strain hardening [6,30]. For the phase stability predictions, another set of aluminum and molybdenum equivalencies were developed and are shown in Eqns. 4 and 5. With both equivalency values, it is possible to predict the approximate phase composition by comparing values against existing alloys with known phase compositions [2].

$$MoE = wt\%Mo + 0.67wt\%V + 0.44wt\%W + 0.28wt\%Nb + 0.22wt\%Ta \quad (4)$$
$$+ 2.9wt\%Fe + 1.6wt\%Cr + 1.25wt\%Ni + 1.7wt\%Mn$$
$$+ 1.7wt\%Co - wt\%Al$$

$$AlE = wt\%Al + 0.17wt\%Zr + 0.33wt\%Sn + 10wt\%O + 10wt\%N \quad (5)$$

MoE and AlE are the molybdenum and aluminum equivalency, respectively. MoE defines the stability of the β phase, and AlE defines the stability of the α phase. Larger values indicate an increase in the phase stability. All wt% terms are the weight percentage of total atomic weight of the respective element. The ranges of MoE values and the corresponding β phase stability are shown in Figure 1.
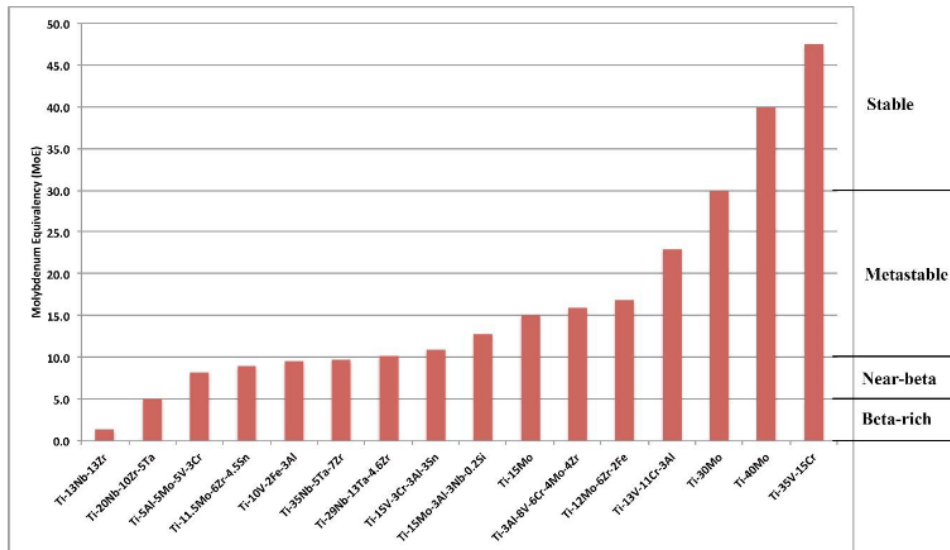
Figure 1: Chart of β Ti phase stability levels, Kolli et al. [2]

The categories of phase stability presented are β-rich, near-β, metastable β, and stable β where the only unrepresented phase stability classes are single phase α, near α, and dual phase α+β. β-rich is defined as a more β stable subclass of dual phase α+β, and it is defined by a primary α phase with a larger amount of β matrix than dual phase α+β. Near-β is defined as almost solid solution β phase structure with small amounts of α phase present, typically these appear during cooling and is less than 5% of phase composition [2]. Metastable β alloys form a solid solution β phase structure that can precipitate out other phases if processed, heated, or loaded. Common precipitates of metastable β titanium alloys are HCP α'-martensite, orthorhombic α''-martensite, and hexagonal or trigonal ω-phase. These precipitates can be controlled via processing like aging, stress induced transformations, and dynamic recrystallization to intentionally harden the alloy [31,32]. Lastly, stable β has a beta transus temperature that is equal to or lower than room temperature, so the β phase is stabilized to the point where precipitation is essentially impossible. These alloys lose the ability to be hardened through phase changes [2,6]. If no β stabilizing elements are present, single phase α is expected. If MoE is approximately zero or less than -10, dual phase α+β is the expected phase composition [2].

2.3 Microstructure influence on creep in titanium alloys

Both α and β phases have unique deformation mechanisms which have an impact on the creep resistance of an alloy. The HCP α phase is a close packed structure with two close packed planes with basal, prismatic, and pyramidal slip systems with families $\{0001\}$, $\{10\bar{1}0\}$, and $\{10\bar{1}1\}$, respectively [33]. Despite only having three primary families of slip systems, the close packed nature of the α phase makes it more ductile and able to have dislocations move relatively easily throughout the lattice [34]. In creep loading, the α phase is dominated by dislocation climb where an edge dislocation moves normal to its slip plane via diffusion [35]. Dislocation climb can either be positive or negative. Positive dislocation climb is a reduction in length of the extra half plane of atoms by an atom leaving the extra half plane and joining the bulk crystal; negative dislocation climb is the opposite where atoms leave the bulk crystal and join the extra half plane

[36]. These processes are both atomic diffusion dependent, so the addition of thermal energy is often needed to begin this process to reach the activation energy for atomic diffusion [36]. This diffusion is also often vacancy and interstitial assisted, so the atoms being diffused into or out of the bulk crystal either want to fill the existing vacancy or escape the interstitial site [36]. Positive climb is filling the vacancy atomic defects and reducing the length of the dislocation line, so this reduces the resistance to dislocation motion as it becomes easier for the dislocation line to advance and grow [36]. Negative climb is removing interstitial defects and increasing the length of the dislocation line, so it is material dependent on what effect the negative climb has on the material although growing the dislocation line typically has the effect of strain hardening the material [36]. The BCC β phase is typically less ductile and less prone to dislocation motion compared to HCP α, especially at room temperature. The BCC crystal lattice has 48 total slip systems on the slip planes {110}, {112}, and {123} [37] of which, none are classified as close packed planes. Without close packed planes, BCC lattices do not slip as readily as HCP lattices and thermal energy is needed to excite the atoms for slip in BCC lattices to reach the level of lattices with close packed planes [38]. As temperature is increased, the BCC lattice reaches the activation energy necessary to allow more dislocation motion, so the ductility of materials with a BCC lattice is often much improved at high temperatures. The activation energy is needed to activate screw dislocation motion in the BCC lattice [38]. The increased dislocation motion improves the ductility of the metal. β titanium is not brittle at room temperature but increasing the temperature has a marked effect on the dislocation motion by allowing more dislocations to be generated and move around within the lattice [38]. As the β phase has less dislocation motion than the α phase, the β phase is noted to have less dislocation climb occur during creep, even at elevated temperatures [9,35,39]. A reduction in dislocation motion results in a decrease in the total plastic deformation a material can undergo before fracture which is generally a negative as being able to store more energy as plastic deformation is beneficial in material design and implementation [40].

The creep resistance of titanium alloys is affected by the microstructural composition. Since the α phase and β phase have different propensities for dislocation climb, there is a non-homogeneous dislocation density throughout the grains. As the dislocations are generated and climb through the α phase, the dislocations will pileup at the α+β phase boundaries. The dislocation pileup eventually leads to stress concentrations at the phase boundaries and can even cause cavitation to occur at the phase boundaries which can lead to crack initiation and propagation [5,28,39]. Single phase alloys avoid these pileups, beneficial in creeping conditions. The α phase, as already established, has dislocation climb as the dominant damage mechanism in creep [35]. The β phase is generally agreed upon to be dominated by GBS in creep [9].

2.4 Room temperature creep of titanium alloys

While creep is most experienced at elevated temperatures, room temperature creep is also possible at higher stresses for many materials. Room temperature creep follows the same regimes as elevated temperature creep: primary, secondary, and tertiary. Primary creep is defined as the initial rapid straining of the material where the strain increases nonlinearly and gradually slows into secondary creep. A power law model for primary creep is the Kachanov-Rabotnov model in Eqn. 6 [5],

$$\left[t_{pr} = A\sigma^{-m} exp\left(\frac{Q_{pr}}{RT}\right) \right] \tag{6}$$

where t_{pr} is the time of primary creep, A is a material constant, σ is the applied stress, m is the stress exponent, Q_{pr} is activation energy for primary creep, R is the gas constant, and T is the temperature. Secondary creep is the simplest part of creep to model and is commonly used as the primary definition of a materials creep resistance as secondary creep is the majority of creep life for most high temperature creeping conditions. This regime entails a linear increase in the strain which gives a constant, minimum strain rate. Secondary creep is also known as steady-state creep for this reason. A model for this regime is Arrhenius law which is a power law model and shown in Eqn. 7 [7].

$$\left[\dot{\varepsilon} = A\sigma^n exp\left(-\frac{Q}{RT}\right)\right] \tag{7}$$

The Arrhenius law is used to describe the secondary creep regime where the steady-state strain rate is $\dot{\varepsilon}$, material constant is A, applied stress is σ, creep exponent is n, activation energy is Q, gas constant is R, and temperature is T in Kelvin to match the gas constant. By repeating creep tests at multiple temperatures and stresses, n, A, and Q can be found for a given material which can then be used to predict the steady-state strain rate at other temperatures and stresses [41]. Tertiary creep is the final regime where the strain rate of the material begins to accelerate again after steady-state creep is complete. The strain rate will continue to increase until the material reaches final fracture. The Monkman-Grant relationship can be used to model tertiary creep and is shown in Eqn. 8 [5],

$$t_f(\dot{\varepsilon}_s)^M = P] \tag{8}$$

where t_f is the time to failure, $\dot{\varepsilon}_s$ is the steady-state strain rate, and M and P are constants for stress and temperature ranges.

Titanium is a material where room temperature creep is noted to occur [39,42–44]. Creep has been measured in titanium at room temperature all the way down to 25% of the yield stress [43]. Furthermore, titanium has been noted to have extremely large creep exponents when modeling using the Arrhenius Law, shown in Eqn. 7 [7,28,42]. Badea *et al.* [7] demonstrates this with Ti-6Al-4V. Despite the applied stresses being 60% yield stress or less, large creep exponents are noted up to 22. Deguchi *et al.* [42] also tested the creep of Ti-6Al-4V but at room temperature. Stresses tested were all around 90% yield stress with extreme creep exponents measured of up to 59. These large creep exponents define the material as in power law breakdown which would invalidate the model. However, published creep data for titanium appears to be a good match to the Arrhenius power law despite the high creep exponents. To compensate for this, a threshold stress, σ_0, is introduced to reduce the creep exponents closer to expected power law

creep exponents of less than 10 as creep exponents equal to or greater than 10 indicate power law breakdown. The modified Arrhenius law is shown in Eqn. 9 [28].

$$\left[\dot{\varepsilon} = A^*(\sigma - \sigma_0)^p exp\left(-\frac{Q_s^*}{RT} \right) \right]$$

(9)

The physical meaning of the threshold stress is the lowest applied stress at a given temperature that will result in a non-zero steady-state strain rate.

GBS is noted to occur in room temperature creep for titanium and its alloys [43,44]. Hemery *et al.* [44] finds that GBS occurs in Ti-6Al-4V in room temperature creep and has a marked effect on local strain fields. The author further asserts that GBS site location can be used to predict crack initiation. Dutton *et al.* [43] notes that GBS occurs at room temperature in another α+β alloy, Ti-6Al-2Nb-1Ta-0.8Mo.

2.5 GBS measurement techniques

GBS is defined as the movement of two grains shearing past each other during creep [16]. Smaller grains are more vulnerable to this phenomenon as it is easier for the grains to rotate and slide around each other [45]. Conversely, larger grains are less vulnerable to this damage mechanism for the opposite reason [45]. Therefore, materials experiencing aggressive creep environments are typically designed to have either large grains or are made from a single crystal, such as gas turbine blades [46].

GBS at an individual grain boundary is not typically a significant damage that will lead to material failure. However, it becomes particularly damaging at triple junctions as the three grains that come together are all trying to slide past each other. The multiple shearing directions lead to void formation [16] as shown in Figure 2 which can lead to crack initiation and eventually crack propagation. Due to the likelihood of this damage mechanism leading to failure, techniques to measure and predict GBS are necessary.
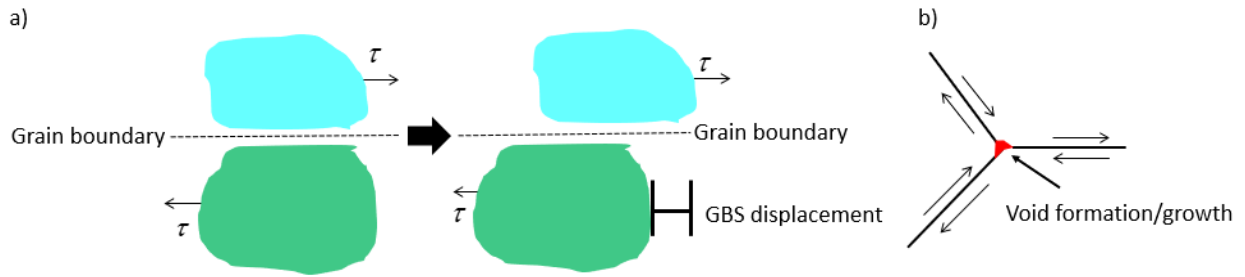
Figure 2: GBS schematics a) GBS occurring in two grains across a single grain boundary b) Void formation due to GBS at triple junction. Adapted from: [47]

The simplest and most common GBS measurement technique is the use of grids applied to the surface of the sample. These grids have been tested at a variety of mesh sizes from 5 μm to 200 μm, depending on sample grain size and equipment used to observe the grids [12,13]. As GBS initiates and propagates, the grid will follow the grain that it is applied to, so the grid will develop discontinuities and angular deflection from 90° segments, shown in Figure 3.
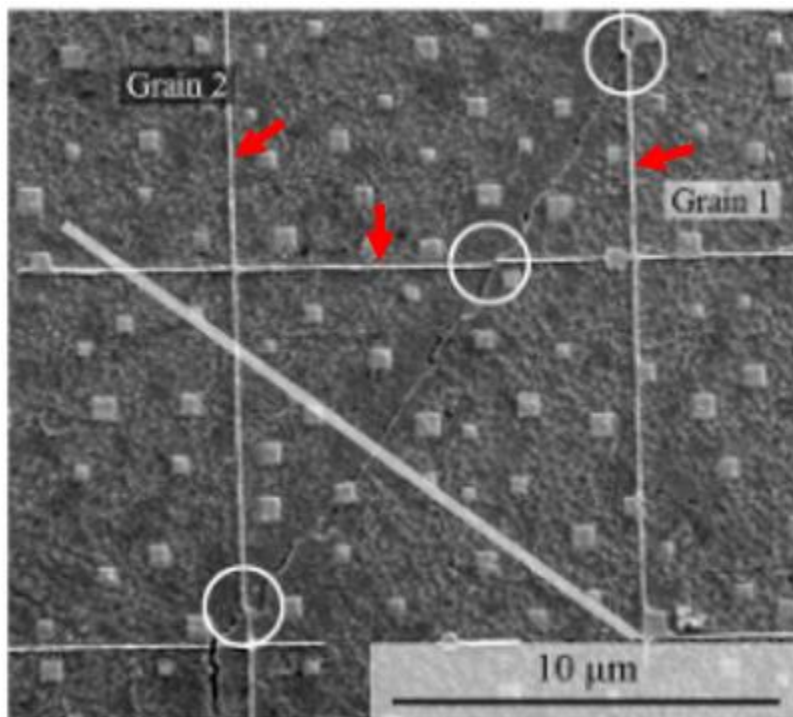
Figure 3: Example of grid used to show GBS with discontinuities circled in white. Source: [12]

The red arrows point to the grid lines applied to the sample surface. The discontinuities circled in white indicate an active GBS grain boundary as the two neighboring grains are sliding past each other. The slanting grid lines shown in Figure 3 indicate the amount of rotation that the grain has experienced. Carter *et al.* [12] used Eqns. 10-12 to quantify the strain associated with GBS,

$$\varepsilon_t = \varepsilon_g + \varepsilon_{GBS} \tag{10}$$

$$\varepsilon_{GBS} = 2n_l \left(\overline{\frac{w}{tan\theta}} \right)_l = n_t (\overline{xtan\theta}) \tag{11}$$

$$\varepsilon_{GBS} = \frac{\bar{g}}{A} \sum s_i n_i \tag{12}$$

where ε_t is the total plastic strain, ε_g is the strain from intra-granular deformation, and ε_{GBS} is the strain from GBS. The discrete offsets of longitudinal and transverse lines are $\bar{w}$ and $\bar{x}$, respectively. The average of the number of grains per unit length of the line for longitudinal and transverse lines are n_l and n_t, respectively. θ is the angle between the tensile axis and grain boundary trace. $\bar{g}$ is the average grain boundary length, A is the area of analysis, s_i is the sliding displacement, and n_i is the normal of the grain boundary projected into the tensile direction. Li *et al.* [13] quantified the shear strain associated with GBS through measuring the angular deflection from 90° developed by the grains in Eqns. 13-15.

$$\varepsilon_{GBS}^{tr} = \frac{\sum W_i}{l_0} \tag{13}$$

$$\varepsilon^{tr} = \frac{l_f - l_0}{l_0} \tag{14}$$

$$\gamma_{GBS} = \frac{\varepsilon_{GBS}^{tr}}{\varepsilon^{tr}} = \frac{\sum W_i}{l_f - l_0} \tag{15}$$

where ε_{GBS}^{tr} is the GBS induced transverse strain, W_i is the overlap length between transverse grid lines, l_0 is the length of coarse grid transverse lines pre-test, ε^{tr} is the total transverse strain, l_f is the length of the coarse grid transverse lines post-test, and γ_{GBS} is the GBS contribution to total strain. The grids used in

these studies needed to be quite precise, so they are applied via FIB in both cases. Carter *et al.* [12] utilized this technique with the creep test running in a scanning electron microscope (SEM) with digital image correlation (DIC), and Li *et al.* [13] used a separate load frame to apply true strain increments where the test was stopped, the sample put in SEM, measured the grid, then replaced in the load frame to reach another true strain increment. This cycle was repeated for true strains of 0.18, 0.36, and 0.54. A second sample is true strained to 0.54, prepped with the grid, and then used for true strains of 0.71, 0.89, and 1.09 which provides an undeformed grid to better measure the GBS at the larger true strains.

Two recent studies have progressed GBS measurement techniques substantially. Linne *et al.* [14,15] developed a more advanced and informative technique that utilizes an initial electron backscatter diffraction (EBSD) generated microstructural map, and then alternating *ex-situ* heating and strain increments with SEM scans of the microstructure to track grain boundary progression. A specialized modular grip is utilized to hold the sample during all stages of the experiment. It maintains zero stress during heating and cooling as thermal expansion was anticipated to be an issue if not addressed. The grip also applied the strain increments used in tensile testing. After the strain increment was applied and the sample cooled, the grip assembly is removed with the sample still in it and placed into an SEM for a full-length scan of the gage section. This process is repeated until the desired strain is reached. By overlaying the initial EBSD microstructural map and the stitched SEM images, the microstructure evolution is tracked at each strain increment. The GBS and slip transmission adjacent to the grain boundary are measured, and grain boundaries are placed into the following categories: GBS without slip interaction, direct transmission with low GBS, indirect transmission, GBS accommodation in polycrystals at triple junctions, and slip activity can influence GBS magnitude gradients. Figure 4 shows the measured GBS along an identified grain boundary.
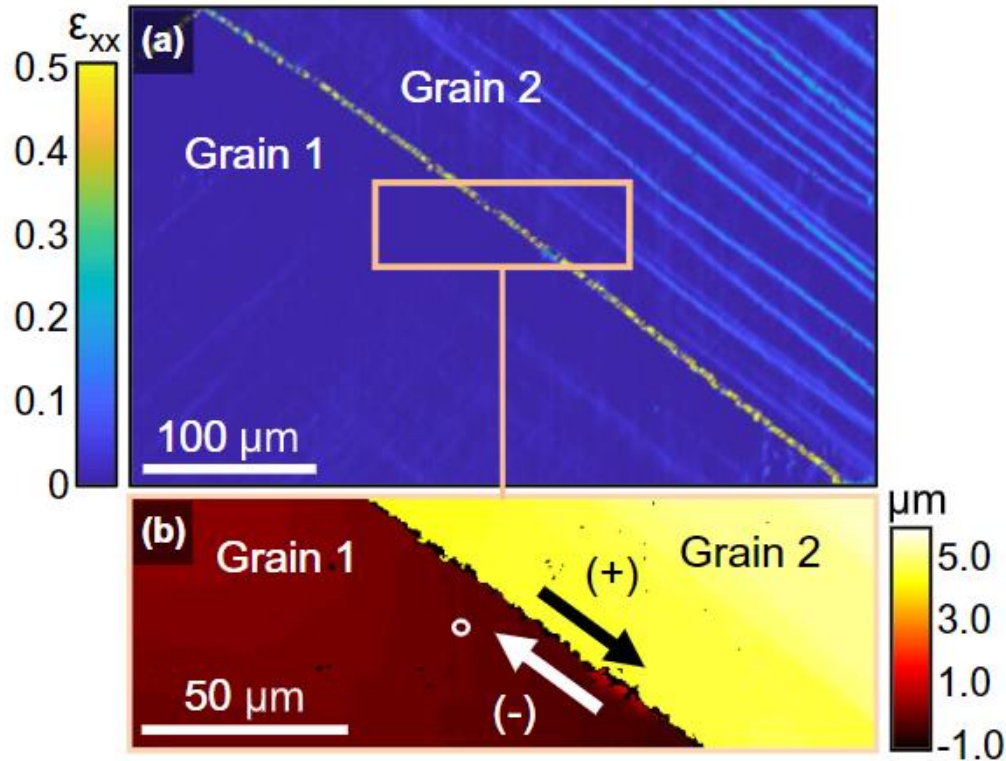
Figure 4: Sample grain boundary a) Strain map around grain boundary b) Displacement gradient displayed around grain boundary. Source: [14]

This technique precisely measures GBS progression by measuring the sliding along the grain boundaries and rotations of the grains to facilitate the shearing along the grain boundaries. The primary drawback of this experimental technique is the thermic cycling used to start and stop the tensile test. This could have an impact on the active deformation mechanism and multiple test interruptions prevents pure tensile test.

2.6 DIC and HRDIC

DIC is a methodology of comparing sequential images and tracking particles as they progressively shift from one image to the next [48]. For mechanical testing, the sample surface is speckled with paint or small particulates to provide a random spread of pixel coloration. Tracking many groups of these speckles at once gives the strain at any point on the sample surface. Averaging the individual strains gives the global strain behavior which is then used to create plots and find material properties. Commercial software

15

packages exist to automatically tabulate these strains, such as Vic-2D from Correlated Solutions, Inc [49]. These can also have image capture software to use in tandem with load frame software to coordinate picture timings, triggering picture taking, load frame data import, and others.

High resolution DIC (HRDIC) is a subclass of DIC where the focus is moved away from global characterization and towards microscale properties [50]. At a much higher magnification, microstructural features can be visible, or their effects can be observed. Tracking particles at this scale creates many possibilities for measuring specific deformation mechanisms. HRDIC has a similar overall process except the particulates used to speckle the sample surface must shrink with the pixel size and the image capturing system must be at a much higher resolution. Common particulates used are aluminum oxide and silica which are air-blasted into the sample surface [48]. Alternatively, gold nano-foils can be used by placing the gold foils on the sample surface and applying a small heat to the foil to cause it to give off small gold particulates that will re-solidify on the sample surface [51]. These speckle patterns are extremely fine and can even be used at the extreme magnification of an SEM.

2.7 EBSD overlaid with Heaviside HRDIC

This thesis developed a new technique for measuring GBS based around overlaying EBSD scan data with HRDIC data and then measuring the discontinuities between two grains via Heaviside function. This is an evolution from existing EBSD and HRDIC overlay techniques [50] with the addition of using a Heaviside function based algorithm to measure GBS. Heaviside functions are designed to not only accommodate discontinuities in data; they are designed to measure discontinuities. Traditional DIC algorithms break down around discontinuities as subset integrity is compromised. Figure 5 shows a DIC algorithm around a discontinuity. The strain map becomes noisy at the discontinuity with jagged pixel displacements and an unclear strain map. These areas must be considered carefully when performing DIC analysis as the introduction of error into global strain is not desired.
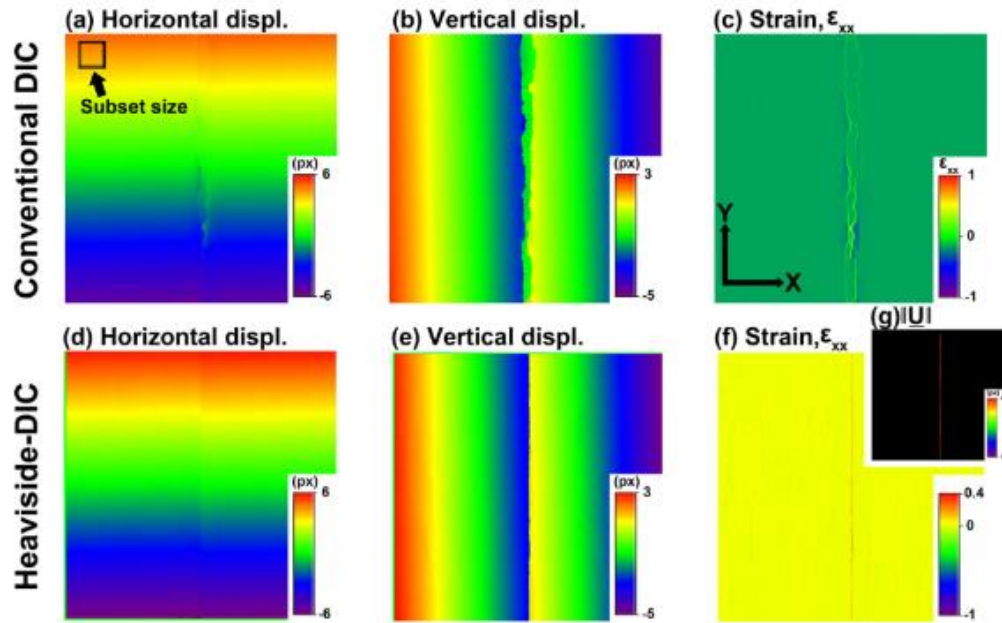
Figure 5: Comparison of conventional DIC (a-c) and Heaviside function based DIC (d-f). Noise shown in conventional DIC (a-c) and reduced noise around discontinuity shown in Heaviside-DIC (d-f). Source: [52]

In addition to noise, DIC algorithms around discontinuities can error out completely so that no data can

be extracted. Figure 6 shows a strain map that has had the DIC algorithm error out at active GBS grain

boundaries.
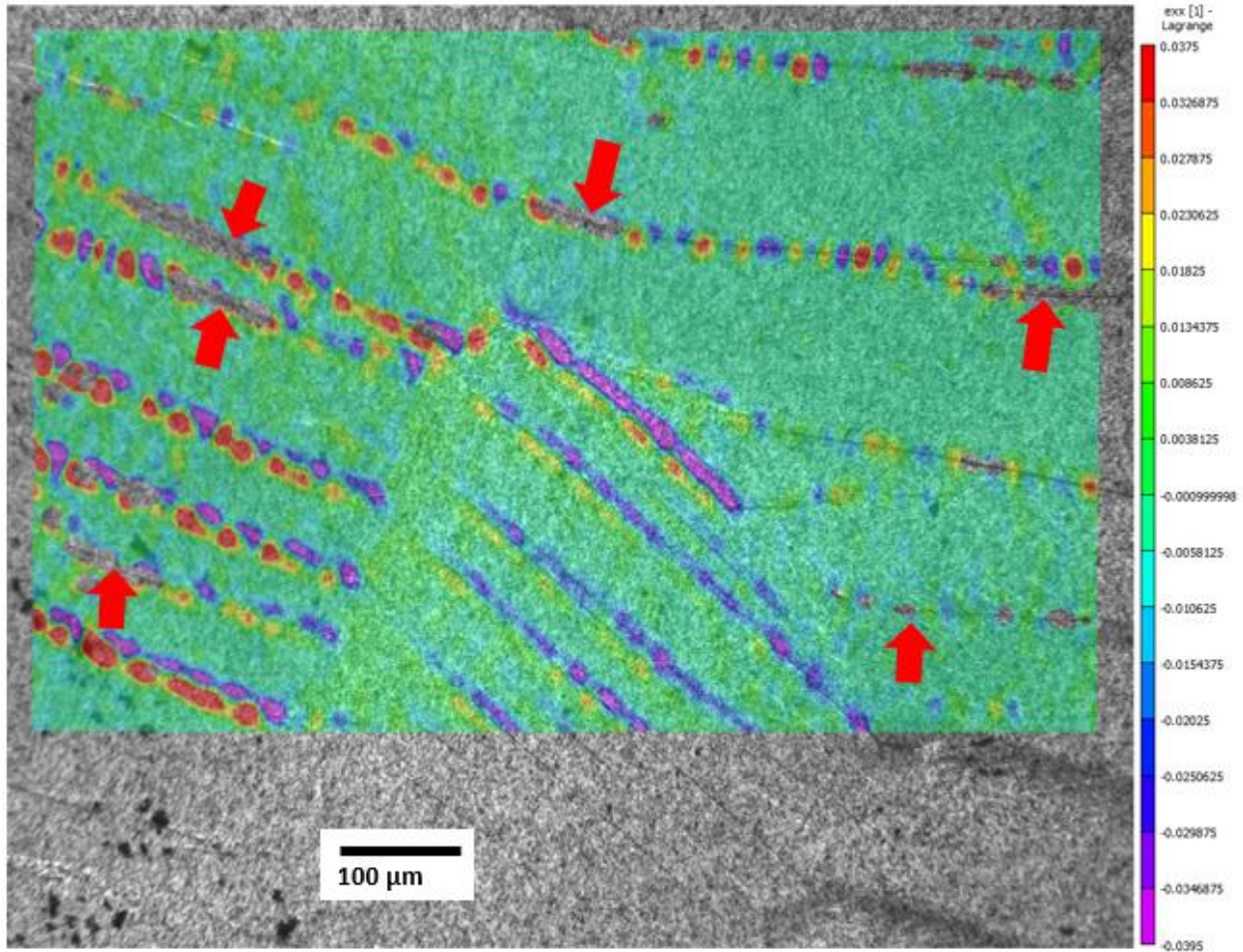
Figure 6: Strain map with failed correlations at discontinuities as indicated by the red arrows.

Heaviside functions are step functions which are theoretically discontinuous as there an instantaneous jump from one value to another. By locating discontinuities and marking the discontinuity location within the subset, the Heaviside function can measure the step of the discontinuity and protect the DIC algorithm from the error it introduces [52,53]. The modification of conventional DIC to Heaviside function based DIC algorithm is shown in Figure 7.
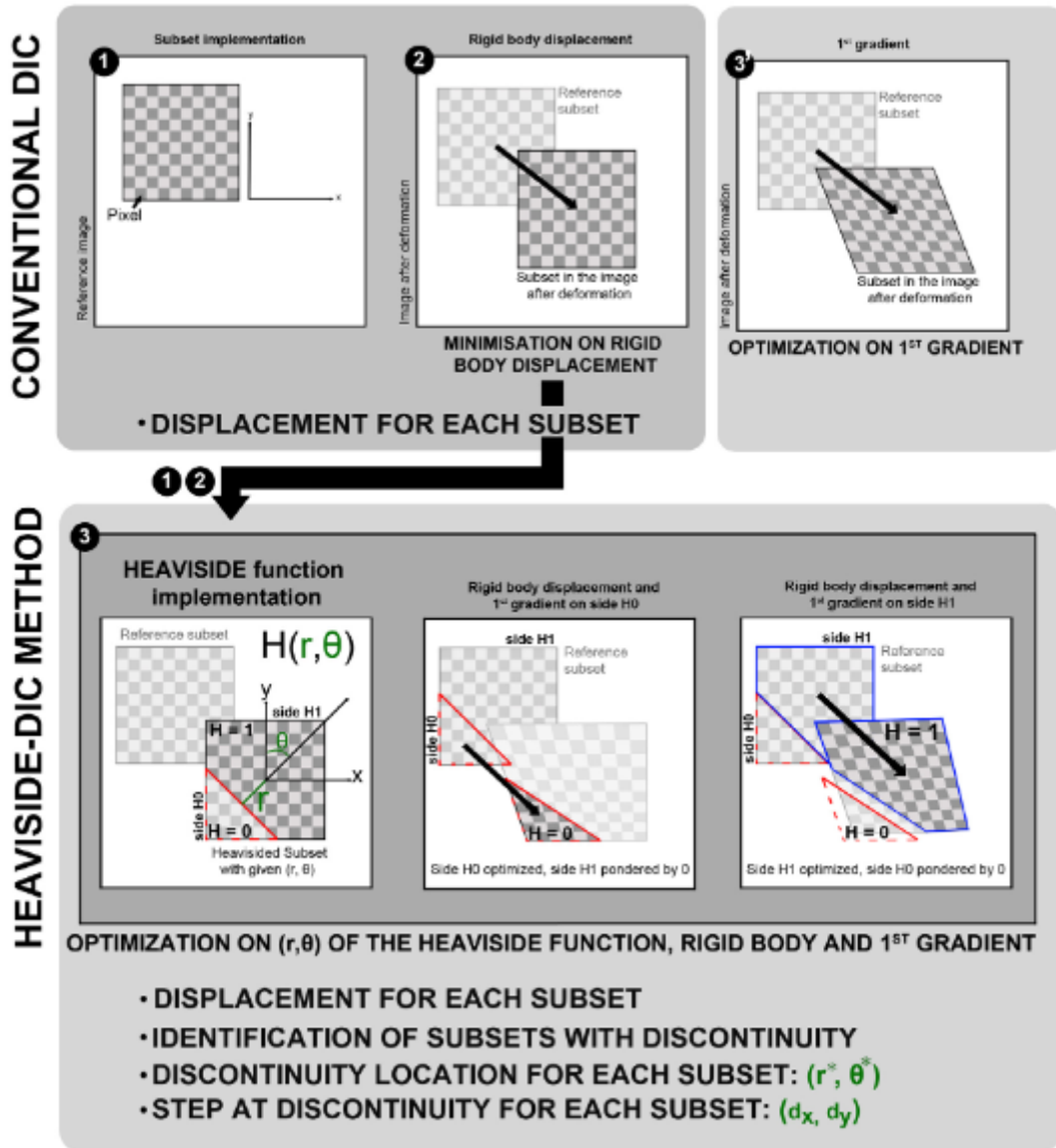
Figure 7: DIC algorithm modification from conventional to Heaviside function based. Source: [53]

These Heaviside function based DIC methods have been proven to work [52,53] for measuring and eliminating errors due to discontinuous microstructures and are implemented as the basis of the measurement technique in this thesis.

Chapter 3.

3.1 Methods and Materials

3.1.1 Materials and sample preparation

The material tested of interest in this study was $Ti_{80}(AlCrNb)_{20}$ which is a Ti-based MPEA initially developed by Liao *et al.* [21]. Material phase composition was approximated via molybdenum equivalency from Eqn. 4 and 5. $Ti_{80}(AlCrNb)_{20}$ theoretically has an MoE of 12.17 and AlE of 3.62 which places it in the metastable categories, so single phase β titanium is the expected phase composition. The material was created in a vacuum, arc-melting furnace with the rough stock shape being disks of approximately 89 mm diameter and 9.5 mm thickness. The disks were cut into dogbone samples via wire electrical discharge machining (EDM) to avoid inducing stress in the sample surface from conventional machining. The dogbone samples had a 2 mm x 4 mm x 30 mm gage section, with the geometry shown in Figure 8. Sample homogeneity was confirmed via energy dispersive spectroscopy (EDS); a sample spectra plot is shown in Figure 9. The averaged compositions are in Table 1. It is noted that EDS measurements were taken at multiple sites with both area and single point measurements taken to ensure homogeneity.

Table 1: EDS averaged measured composition

Element	Expected at%	Measured at%
Ti	80	79.8±0.4
Al	6.66	7.0±0.3
Cr	6.66	6.8±0.1
Nb	6.66	6.4±0.2
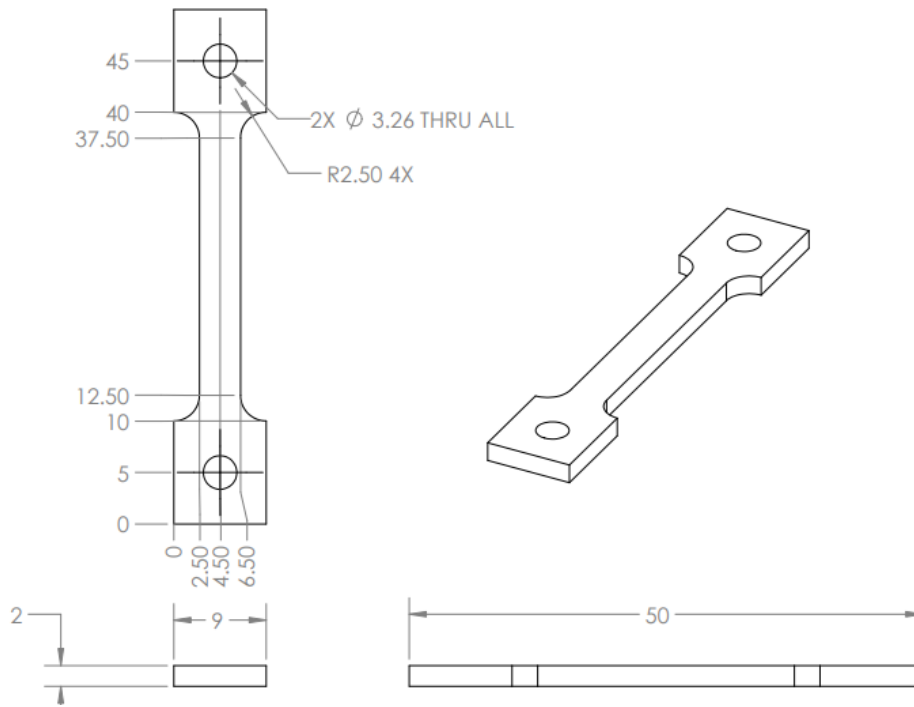
Figure 8: CAD drawing of dogbone sample
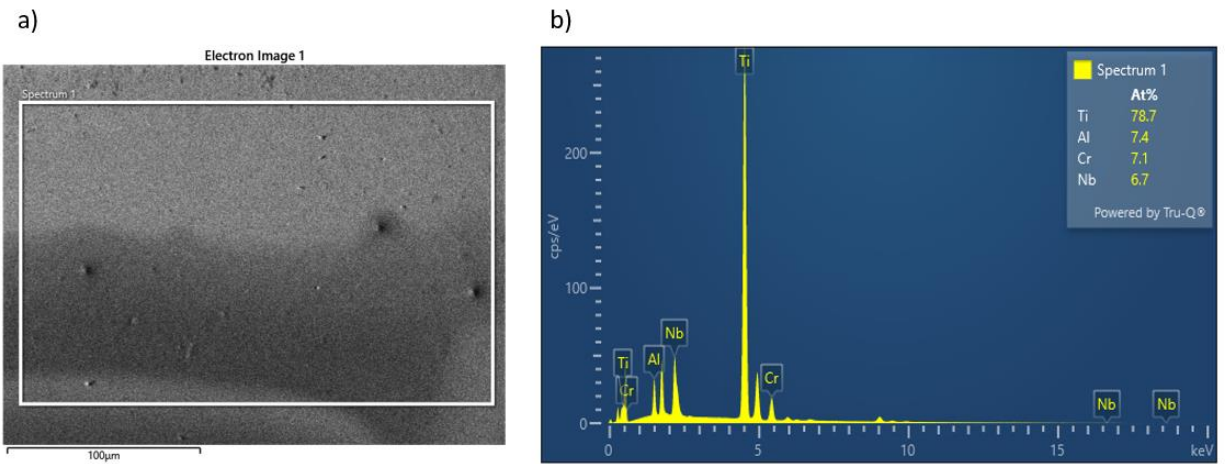
Figure 9: a) EDS capture region b) Associated spectrum plot

It is noted that the measured compositions were used to re-calculate the MoE and AlE to be 12.25 and

3.81, respectively. This maintains the approximated phase composition of single phase, metastable β.

Samples were tested with two different solutionizing treatments (ST): 0.25 hours and 12 hours at 1100°C

in an inert environment followed by immediate water quenching to maintain solid solution β Ti

microstructure [21,54,55]. Encapsulation setup used to create inert environment for samples, shown in Figure 10.
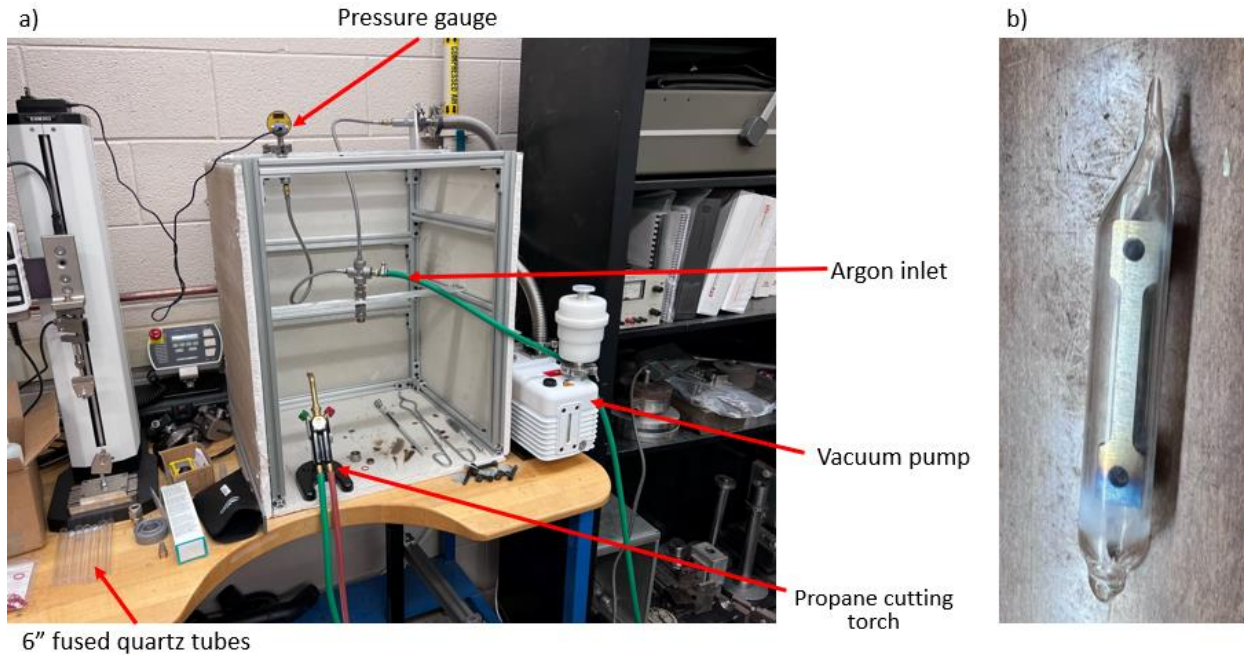
Figure 10: a) Encapsulation setup with red arrows pointing out key components b) Completed capsule

Encapsulation setup uses fused quartz tubes that are heated with a propane cutting torch until soft enough to draw out and neck down tube diameter until seal is completed. The vacuum pump, argon, and pressure gauge are used to control the gas composition within the gas lines and capsule. Encapsulation process is as follows:

1. Neck down bottom of 6" fused quartz tubes and place sample inside

2. Connect tube to gas lines with vacuum fitting

3. Neck down top of 6" fused quartz and seal bottom

4. Cycle between vacuum pumping out air and backfilling argon gas

5. Seal top of 6" fused quartz tube

It is noted that lowest air pressure measured was 300 mTorr which classifies as low vacuum. By backfilling with argon, pressure within the gas lines is approximately equalized with surrounding air pressure which makes the final seal at the top of the capsule easier. Completed capsules can then be placed into an open-air furnace for ST. Water quenching is done by dropping capsule into water bucket directly from ST in furnace. Grain sizes measured for each ST, shown in Table 2.

Table 2: Measured grain sizes of ST $Ti_{80}(AlCrNb)_{20}$

Solutionizing treatment	Grain Size [µm]
12 hr ST	406
0.25 hr ST	261

It is noted that these measurements are not fully representative of the microstructure as much larger grains are visible on the sample surface; some of which are on the order of a millimeter. 1100°C ST temperature chosen from Lin *et al.* [55] to treat at a super beta transus temperature to create solid solution β titanium microstructure. 12 hr ST was chosen from Liao *et al.* and Lin *et al.* [21,55], and the 0.25 hr ST was chosen from Rajan *et al.* [54] as a more optimal treatment for mechanical properties. Longer than 0.5 hr ST at super beta transus is noted to degrade mechanical performance [2,54]. The dogbone samples are held in an inert environment during ST and water quenched from 1100°C to maintain single phase β microstructure during cooling. Rajan *et al.* [54] also notes that aging after ST to grow α, α', or α'' precipitates is recommended to fully optimize mechanical properties; however, aging was skipped for $Ti_{80}(AlCrNb)_{20}$ as a solid solution β titanium microstructure is desired both for creep properties and for Heaviside function based algorithm development. One sample received an additional step of aging at 440°C for 8 hr to maximize yield strength for a monotonic tensile test [54].

3.1.2 Testing equipment and speckle applications

Dogbone samples were tested in both monotonic tension and tensile creep on 100 kN hydraulic MTS frame and 10 kN Psylotech ball screw driven frame shown in Figure 11. All samples were speckled with

the samples to be used on the 100 kN hydraulic MTS frame using paint airbrush applied high-temp ceramic black mixed with acetone in a 30/70 ratio, respectively, and the samples tested on the 10 kN Psylotech ball screw driven frame using 1200 mesh aluminum oxide powder air blasted into the sample surface. These speckling techniques and materials were selected as the particulates are appropriately sized for their respective camera and lens setup, shown in Figure 12. The 100 kN hydraulic MTS frame used a Navitar 1-60135 lens for DIC, and the 10 kN Psylotech ball screw driven frame used an Olympus SLMPLN20X for HRDIC.
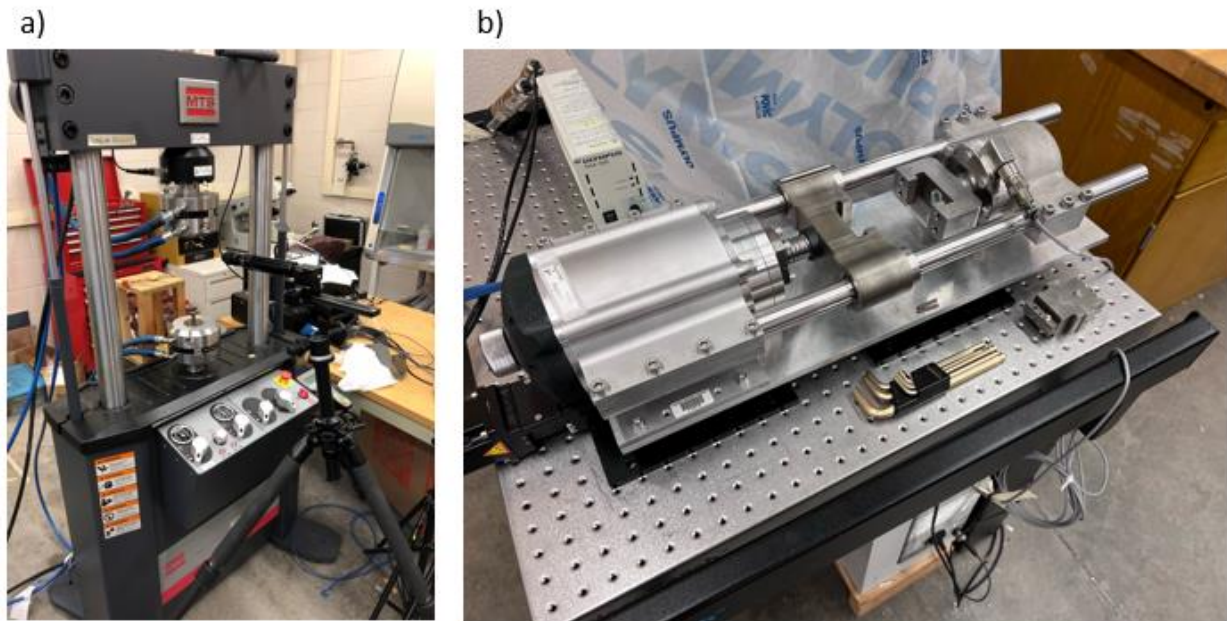
Figure 11: a) 100 kN hydraulic MTS frame b) 10 kN ball screw driven Psylotech frame
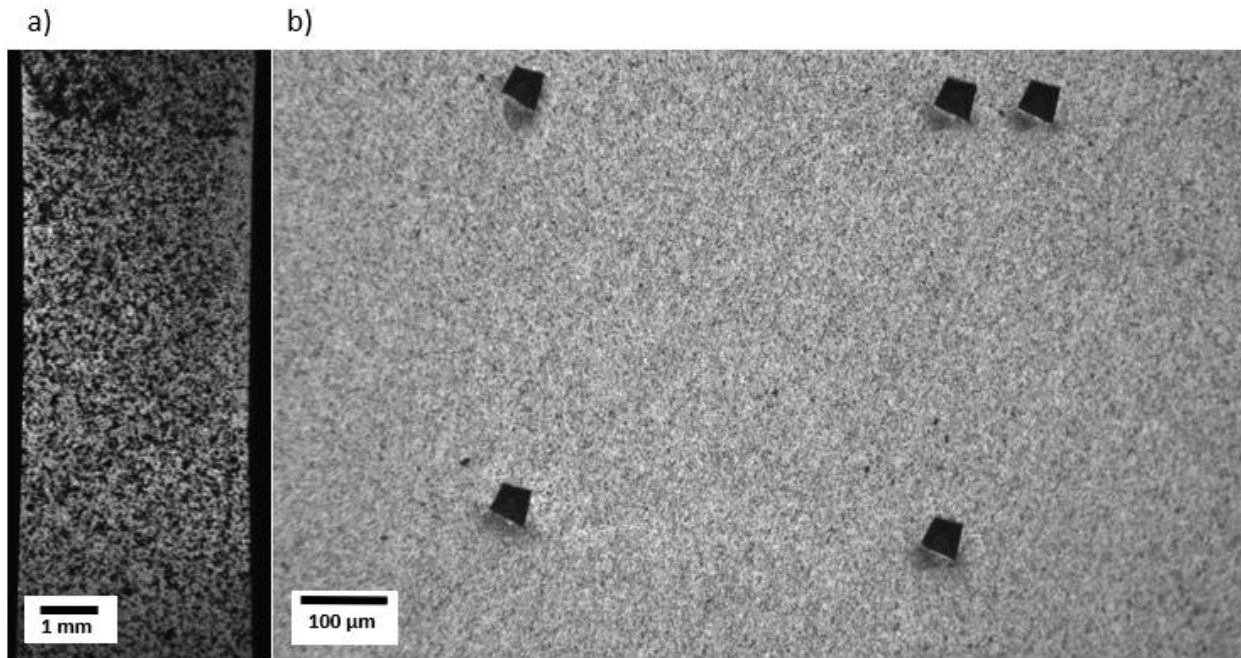
Figure 12: Sample speckle patterns a) 30/70 acetone/high temperature ceramic paint b) 1200 mesh aluminum oxide

3.1.3 Tensile testing setup

Monotonic tensile tests were performed at a strain rate of 2×10^{-4} s^{-1} which translates to a displacement rate of 6 µm/s for the 30 mm gage section. The global strain of the sample was measured via DIC with forces captured from load cell readings. These tests were run until fracture to capture both elastic and plastic behaviors.

Stiffness tests were run as well to confirm elastic behavior, specifically the Young's modulus. These stresses used in the stiffness tests were as follows: 0 MPa, 320 MPa, 25 MPa, 320 MPa, and 0 MPa in that order, where 320 MPa is half the measured yield stress and 25 MPa is used to maintain pin engagement on the sample. These tests were run at the same strain rate and displacement rate as the monotonic tensile tests with the overall displacement derived from reaching 320 MPa using a known stiffness. Hooke's law, Eqn. 16, is used to define displacement from given stresses.

$$E = \frac{\sigma}{\varepsilon} \tag{16}$$

The global strain for the monotonic tensile tests was calculated via DIC which averages the local strains to find ε_{xx}, ε_{xy}, and ε_{yy}. The forces were taken from the load cell data and converted into stress via sample gage section measurement. These are combined to plot engineering stress in Figure 18 and the mechanical properties in Table 3.

3.1.4 Creep testing setup

Creep testing was performed on the 10 kN ball screw driven Psylotech frame to enable HRDIC. The creep tests were performed under load control conditions through primary and secondary creep. The load selected was the proportional limit from the monotonic tensile testing, which is 544 MPa and 85% of the yield stress. This load was selected as it is the bottom end of the suggested load for room temperature creep of Ti that will not require more than 500 hours to rupture [42,43]. As microstructure damage measurement technique development is the primary goal of this thesis, the creep test applied stress was selected to be long enough for $Ti_{80}(AlCrNb)_{20}$ to experience GBS and other localized damage gradually enough to be captured optically but also short enough that testing would not be excessively long. A higher stress of 576 MPa and 90% yield stress was also tested to compare against.

The data from these creep tests was also for used in the GBS analysis code, so the test setup was designed to provide the data needed to characterize creep behavior and then develop and implement the GBS measurement technique. To prepare for creep testing, sample surface is marked with five fiducial markers with either 300 or 500 µm spacing in a square with a fifth marker placed to identify orientation, shown in Figure 13.
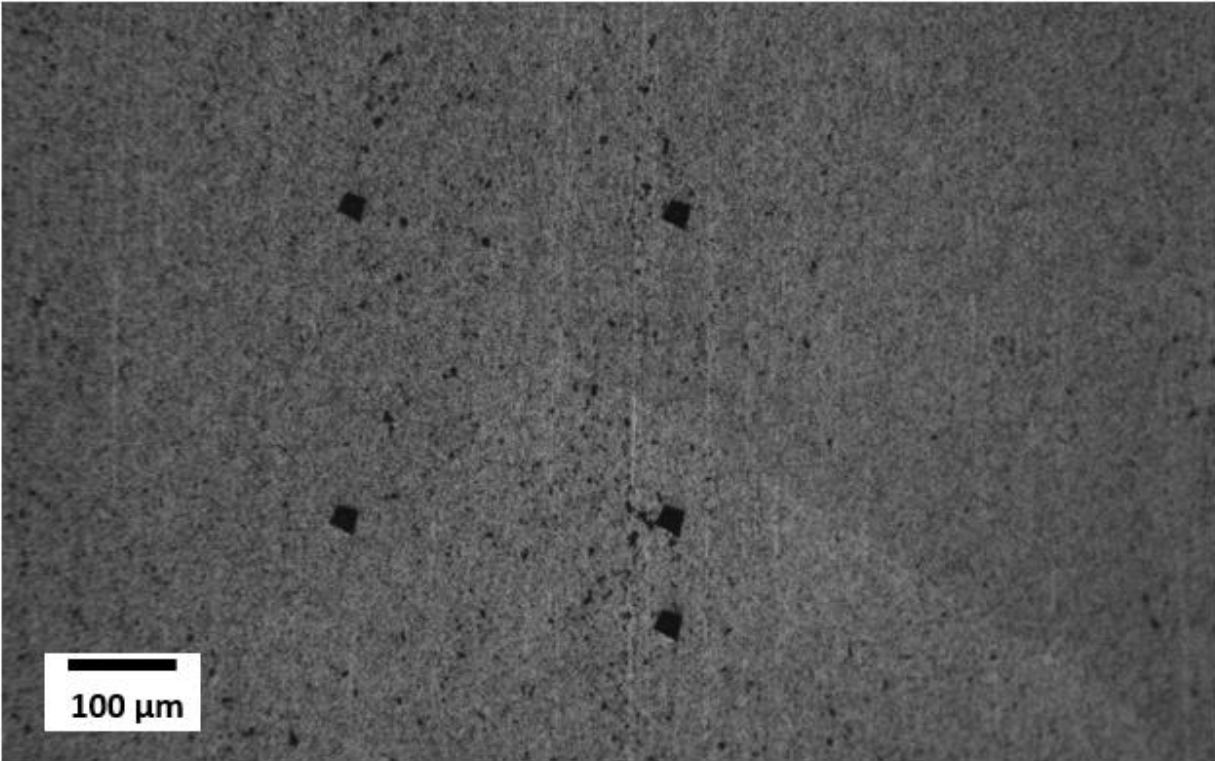
Figure 13: HRDIC image of fiducial marked sample

Fiducial markers are placed with a Vickers hardness tester with a 400 g load applied through a diamond tip. The markers are placed after sample surface is polished for EBSD from Buehler titanium polishing guidelines: 320 grit silicon carbide paper until plane, UltraPad with 9 μm diamond suspension for 10 minutes, and MicroCloth with 0.5 μm colloidal silica attack solution for 10 minutes. Next, an EBSD scan on a Hitachi SU5000 at Clemson University's Advanced Materials Research Laboratory to capture the microstructure at the fiducial markers is taken. Due to rapid oxide layer formation of $Ti_{80}(AlCrNb)_{20}$, the final polishing step of the MicroCloth with 0.5 μm colloidal silica attack solution is repeated for 15 seconds to remove the oxide layer, and the sample is then immediately placed into the vacuum environment of the SU5000. An example of this scan is shown in Figure 14.
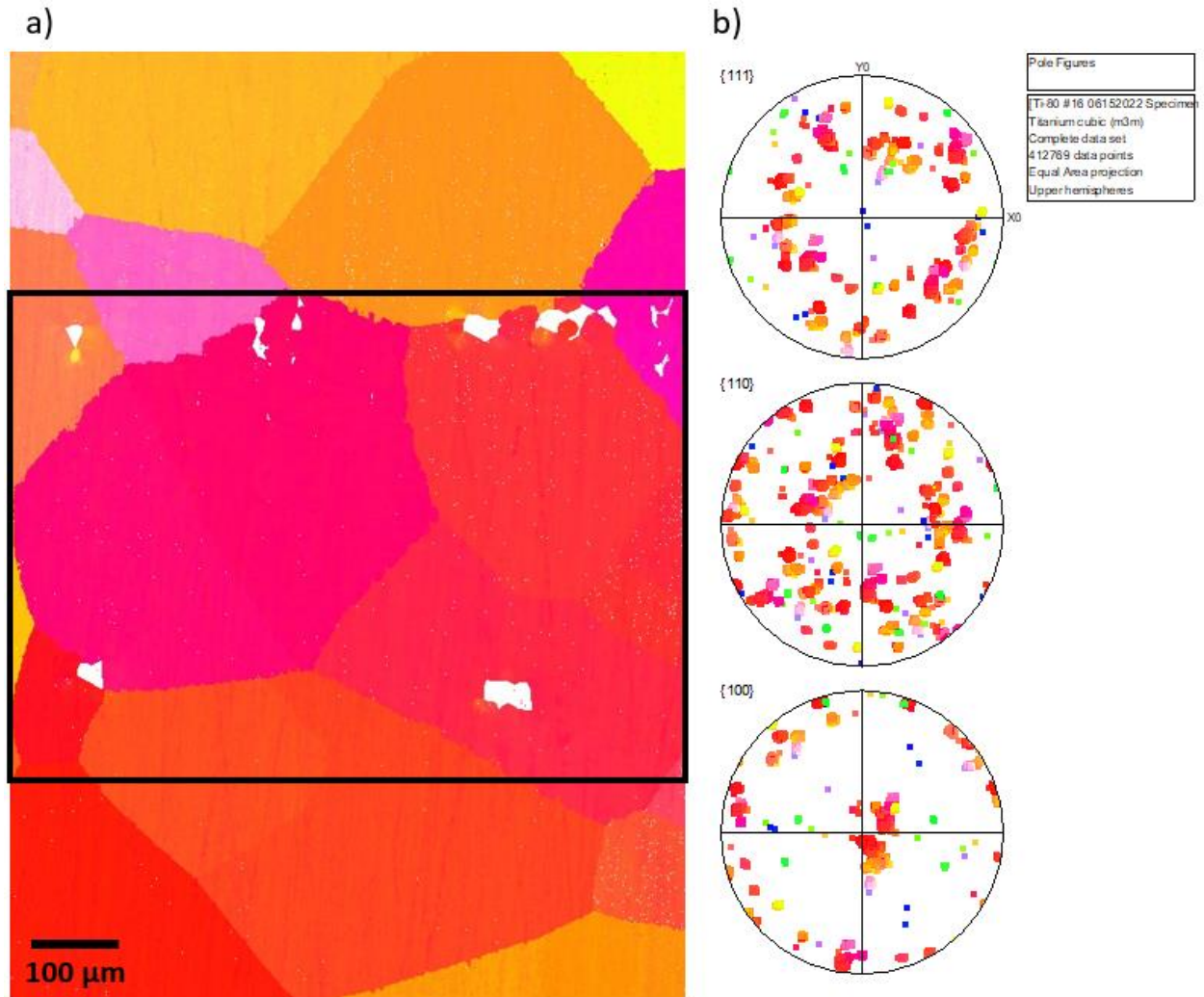
Figure 14: a) EBSD scan of fiducial marked sample. Black box indicates area used in GBS analysis code b) Pole figures of EBSD scan

3.2 GBS analysis code development

The GBS analysis code was implemented in MATLAB to incorporate MTEX [56], a toolbox for analyzing crystallographic textures. The overall procedure for this analysis is:

1. Overlay EBSD and reference HRDIC image with fiducial markers aligned

2. Compute strain maps in Vic-2D and export DIC data to MATLAB

3. Apply Heaviside function based algorithm to measure discontinuity across grain boundaries

MTEX is a software package that can import, process, and manipulate EBSD/SEM data in the standard formats: .ctf, .cpr, .crc, etc. The data includes all the Euler angle data and the associated locations for each. This data can then be immediately plotted to match the output from the SEM which will include the non-indexed points from the scan as well. Many options exist for plotting EBSD data: phases, orientations, grains, and grain boundaries can all be plotted individually or overlaid to better see features such as grain boundaries around phases. To prepare for overlaying the EBSD and HRDIC data, the EBSD data is cleaned up to remove non-indexed data and other noise, like misidentified phases, while leaving clear fiducial markers intact. The MTEX data cleaning technique is based on grain detection, so grain size or the ratio of grain size to boundary size are used to determine the grains to be removed. During cleaning, when the software detects excessively small grains, they are most commonly non-indexed data or misread phases resulting in no data lost by removing them. The cleaned data is then converted into an image for fiducial marker alignment. The HRDIC data is also imported and converted into an indexed grayscale map for each image to prepare for overlaying with the MTEX processed EBSD data.

Next, the fiducial markers in the EBSD image and reference HRDIC image are aligned. This was done graphically for accessibility and potential variability in data sets. MATLAB has built in image transformation tools for aligning images that have been rotated, translated, and scaled which were used in this analysis code. Using the selected points on the EBSD and HRDIC figures, MATLAB finds the necessary transformations that need to be applied to approximately align the fiducial markers. These transformations are recorded and are applied to the EBSD image to transform it to align with the reference HRDIC image, and the two images are plotted on top of each other to confirm alignment.

The strain maps from traditional DIC were generated via Vic-2D. All images to be analyzed were loaded into Vic-2D with the first image being the image that all subsequent images were compared against, also known as the reference image. A step size of 5 was selected which means Vic-2D will perform a correlation every 5th pixel. This step size is refined enough to have detailed strain maps while keeping computational

load manageable. Selection area is as large as possible to give as complete of a strain map as possible. The

subset size was set as low as possible while maintaining strain map integrity to capture local strain

concentrations. If the strain map broke down past the immediate vicinity of discontinuities, then the

subset size is increased until the strain map integrity was satisfactory. Smaller subsets are more desirable

for the Heaviside function implementation, but if the subset size was too small, the strain map will

degrade in other locations. Subset size typically ranged from 361 to 961 pixels^2 for the experimental setup

used. The initial guess was placed away from discontinuities and checked to confirm that the subset

tracking was viable at the selected settings. Strain computation was performed with a filter size of 5 which

defines the virtual strain gauge and tensor type of Lagrangian. The virtual strain gauge links sequential

subsets to measure how they move in relation to each other. With a filter size of 5, the center subset is

connected to two subsets to the left, right, up, and down. The displacements between each subset are

measured to generate ε_{xx}, ε_{yy}, and ε_{xy} for the center subset. These strains are shown locally in the strain

maps and can be averaged to find global strain. DIC parameter selection is based on best practices from

Bigger *et al.* [57] and Correlated Solutions, Inc. [49]. All data generated is exported into .mat files to

simplify MATLAB import; however, other export types such as .csv would be acceptable.

The data is imported into MATLAB and includes x and y location in pixels, u and v which are the horizontal

and vertical displacement from reference in pixels, sigma which is the 1-standard deviation confidence in

the pixel match of the specified pixel, the local strains in ε_{xx}, ε_{yy}, and ε_{xy}, and principal strains ε_1 and ε_2.

Eqns. 17-19 are the formulas used by Vic-2D to calculate the Green-Lagrangian strain tensor [49].

$$\varepsilon_{xx} = \frac{du}{dx} + \frac{\left(\frac{du}{dx}\right)^2 + \left(\frac{dv}{dx}\right)^2}{2} \tag{17}$$

$$\varepsilon_{yy} = \frac{dv}{dy} + \frac{\left(\frac{du}{dy}\right)^2 + \left(\frac{dv}{dy}\right)^2}{2} \tag{18}$$

$$\varepsilon_{xy} = \frac{\dfrac{du}{dy} + \dfrac{dv}{dx} + \dfrac{du}{dx}\dfrac{du}{dy} + \dfrac{dv}{dx}\dfrac{dv}{dy}}{2} \tag{19}$$

The ε terms are defined as the local strains in their respective directions with ε_{xx} and ε_{yy} being normal strains and ε_{xy} being the shear strain in 2D. The differential terms for u and v are the changes in pixel location with respect to x and y from the reference image pixel location. The imported data is then plotted as an image progressively to observe the discontinuities and how they appear in the various data types, shown in Figure 15.
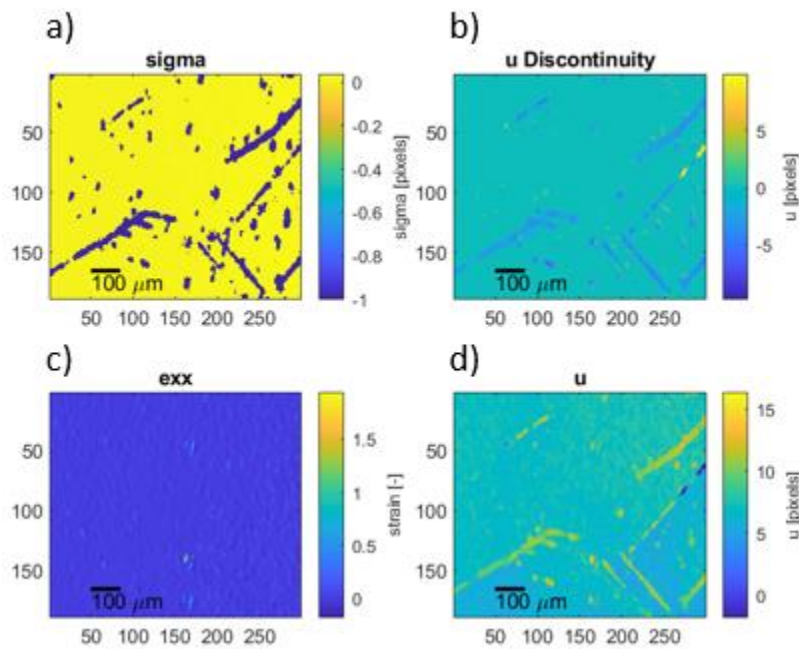
Figure 15: Plots from DIC output of final image a) sigma values b) u discontinuity measurement c) ε_{xx} map d) u displacement map

Vic-2D does not have a direct indicator for discontinuities, but sigma indirectly acts as one. Sigma being set to -1 indicates a high level of uncertainty in the correlation, and discontinuities create high levels of uncertainty in the correlation. Other points can also have these large uncertainties, but it is most common in discontinuities. These points are clearly visible as the sections with strong color contrast in Figure 15a and will be used for discontinuity indexing. Figure 15b shows an attempt to measure discontinuities

without the use of discontinuity size and noise reduction from Heaviside function or any other processing. This plot is derived from defining a subset around a discontinuity point of 2601 pixels^2 and averaging the surrounding u values in the subset to quantify the discontinuity of the selected point with the surrounding area. 2601 pixels^2 is selected as it was found to be a large enough subset to avoid the average u being overly influenced by discontinuity and small enough to be limited to capture localized behavior. As seen in Figure 15b, this adds little value compared to the other plots in Figure 15, and there is significant variation in discontinuities measured which makes the output difficult to use to quantify microstructure deformation. Another issue with using this methodology is GBS quantification is going to be overly complicated. As the discontinuities have varying widths and heights, it will be unclear on the plots where the GBS measurements are precisely located.

To improve discontinuity measurements, the discontinuities are compressed into a single line to best locate the slip trace or grain boundary centers. The processing used for this is scanning through the sigma values of each image column by column to find the -1 values that indicate a discontinuity, and the discontinuities are indexed sequentially down the columns of the DIC data. The indexes of each discontinuity are then averaged to find the discontinuity center. For discontinuities with an odd number of pixels, this will return the center without further processing. For discontinuities with an even number of pixels, a random integer is generated which decides whether the center will be the upper or lower integer to avoid biasing the discontinuities up or down in the image in the aggregate as there is a theoretically even chance of either being selected. The compression into a single pixel is used to simplify the visual representation of these discontinuities; alternatively, compression could be skipped, and the discontinuity measurement plotted across the entire width of the detected discontinuity. There will be discontinuities at the edges of the Vic-2D, so the discontinuity compression algorithm was protected against these by breaking the discontinuity searching loop if the edge of the data is detected. Figure 16 is a sample output of the discontinuities after full discontinuity compression.
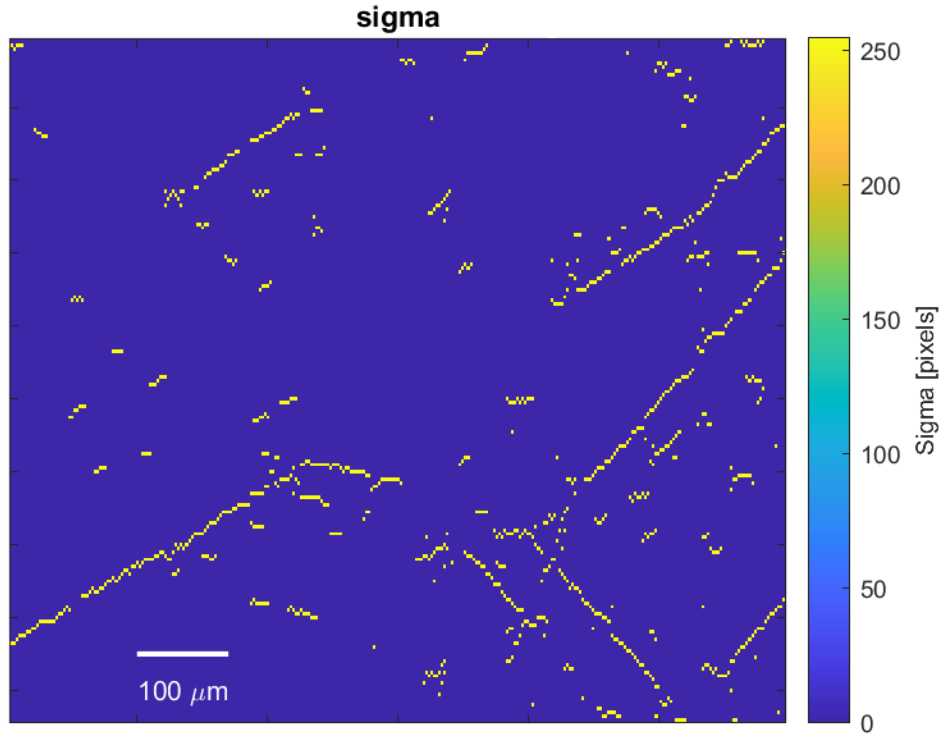
Figure 16: Final image with discontinuity compression applied and sigma values set to 255 to maximize contrast with continuous pixels

The discontinuity compression leaves only single pixels behind in each column of the DIC output, so the output can appear jagged. This compression also does not differentiate between intragranular slip traces and grain boundaries, so there is more processing needed to identify each. This method of discontinuity identification and compression deviates from the subset-based Heaviside function utilized by Stinville *et al.* and Bourdin *et al.* [52,53]. This is due to a difference in DIC usage. The subset-based Heaviside function was designed around building a Heaviside function based DIC algorithm that actively compresses discontinuities as it detects them. The technique developed in this thesis relies on a commercial DIC software package, Vic-2D, that does not lend itself well to being processed into subsets after completing the conventional DIC algorithm. Subset processing post DIC completion would involve dividing data into subsets and identifying the discontinuities within each subset to then stitch the complete data set back together. The problem arises as issues are created both by small and large subsets. Small subsets would likely only have one discontinuity, but there is no guarantee that the discontinuity would be entirely

33

contained within the selected subset which would cause a discontinuity to be erroneously split apart. Furthermore, identifying and indexing discontinuities at corners of subsets would be very problematic as neighboring subsets would need to be included to verify size and direction. Large subsets would be unlikely to split discontinuities or have them at corners, but they would be more likely to capture multiple discontinuities which would significantly complicate the discontinuity identification. These factors made a full image scan a much more appealing solution than working through the issues with a subset-based method to imitate existing work [52,53]. The efficiency and common use of commercial DIC software packages makes the developed technique easier for wide-spread adoption. Therefore, the method of discontinuity compression and quantification presented in this thesis utilizes scanning the full image and not smaller subsets. It is also noted that this method of discontinuity location and compression will not work with vertical discontinuities as scanning the columns would compress an entire length of discontinuity into a single point which is incorrect. Future codes will address this issue.

During discontinuity compression, the discontinuity boundaries are also located and plotted in Figure 17.
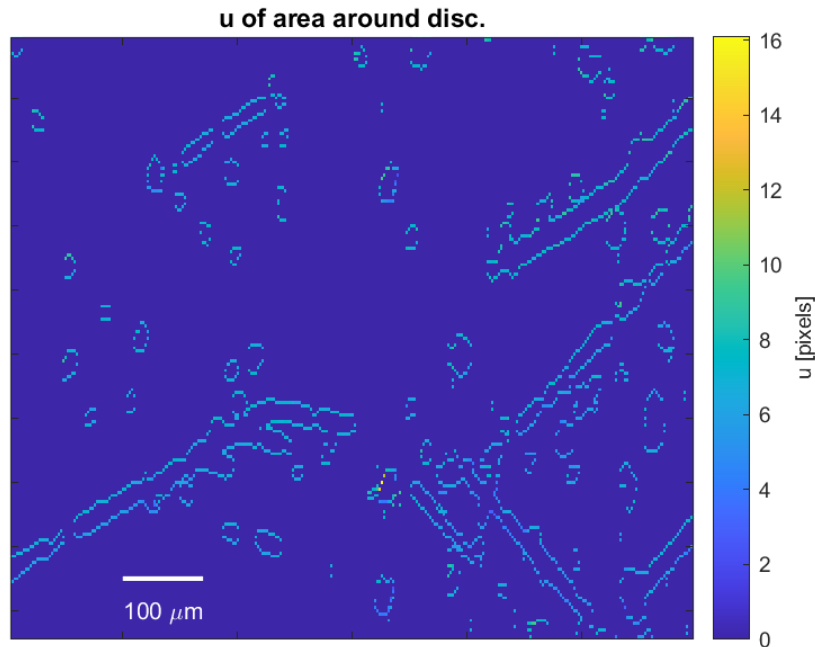
Figure 17: Plot of the of x displacement of the pixels surrounding discontinuities

These boundaries are defined as the points immediately above and below a discontinuity where sigma is not equal to -1. These indexes will be used to measure the displacement across the discontinuity. Since they were the first points that Vic-2D did not recognize as discontinuous, the displacement values measured should better represent the movement of the bulk crystal in the grain. By comparing the pixel displacements at these points and converting them into µm, the GBS across grain boundaries and discontinuity around slip traces can be calculated by comparing measured discontinuities back to the overlaid EBSD and reference HRDIC image. After the GBS measurement is complete, the analysis code outputs are compared against a virtual extensometer from Vic-2D to validate the code measurements.

3.3 Results and Discussion

3.3.1 Tensile and stiffness test results and discussion

Tensile tests had varying results based on the chosen ST. Figure 18 shows the monotonic tensile plots, and Table 3 shows the corresponding measured mechanical properties from tensile and stiffness tests.
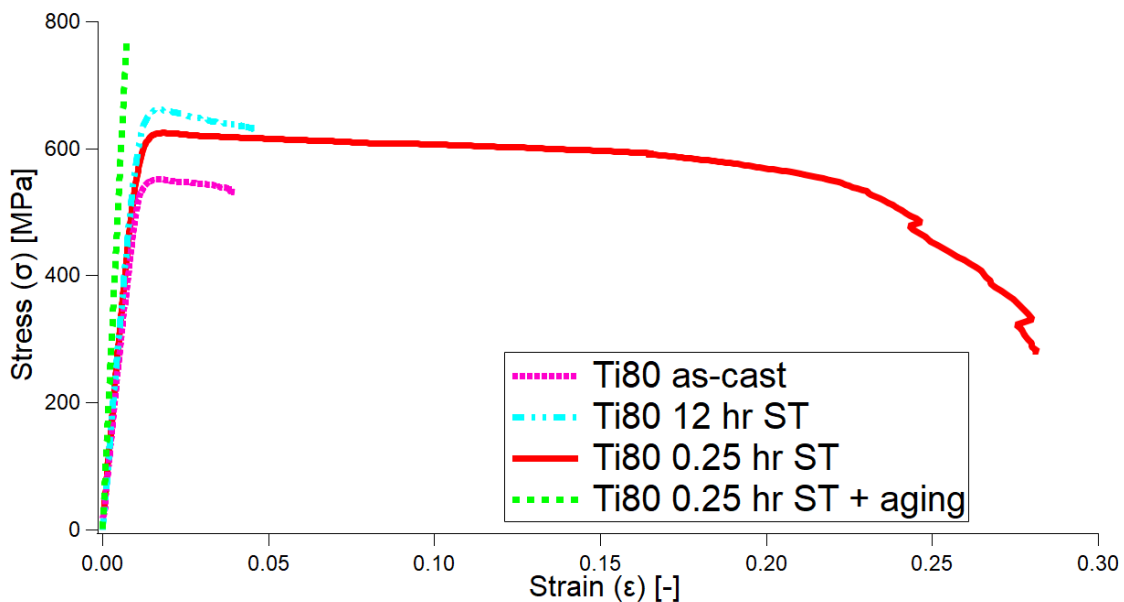
Figure 18: $Ti_{80}(AlCrNb)_{20}$ monotonic tensile test results

Table 3: Mechanical properties from monotonic tensile tests

Solutionizing treatment	Stiffness (E) [GPa]	Yield Stress (σ_y) [MPa]	Strain [-]
As-cast	51.5	540	0.040
12 hr ST	61.2±0.4	640	0.046
0.25 hr ST	58.5±1.4	620	0.282
0.25 hr ST + 440°C 8 hr aging	110.3	-	-

The $Ti_{80}(AlCrNb)_{20}$ as-cast samples had the poorest mechanical properties with low yield stress and poor ductility. The stiffness was also low, but this aligns with common biomedical titanium implant alloys where lower stiffness closer to that of bone are desired [3]. The 12 hr ST samples have improved properties with increases in stiffness, yield stress, and strain of 9.7 GPa, 100 MPa, and 0.006, respectively. The 0.25 hr ST samples have similar improvements from the as-cast sample with an increase in stiffness, yield stress, and strain of 7 GPa, 80 MPa, and 0.242, respectively. At a small reduction in stiffness and yield stress improvement, the ductility of the 0.25 hr ST samples is vastly improved which is in line with expectations as this is the optimal super beta transus ST treatment for metastable β titanium alloys [2,54]. However, these improvements do not move the alloy in line with commercial titanium alloys. The primary issues were the yield stress being far below expected values, perfectly plastic behavior, and softening. The yield stress was approximately 300 MPa below expected values [3]. Perfectly plastic behavior is not unexpected for metastable β titanium with grains of this size [6], but the addition of softening is bad for alloy performance. An aging treatment of 440°C for 8 hr was attempted to optimize yield strength and stiffness for $Ti_{80}(AlCrNb)_{20}$ while maintaining some of the ductility seen in the 0.25 hr ST sample [54]. The aging introduced α phase precipitates that increased the yield stress and greatly increased the stiffness; however, the aging also embrittled the alloy as it displayed brittle behavior. Based on the CALPHAD plot for $Ti_x(AlCrNb)_{100-x}$ from Liao *et al.* [21] shown in Figure 19, both α and intermetallic, cubic laves phases are predicted at the this temperature. These contribute to increasing the stiffness to be in line with

annealed Ti-6Al-4V [3] and embrittlement due to intermetallic laves phases. This sample also fractured in the grips, so the measured max stress is not reported as the yield stress.
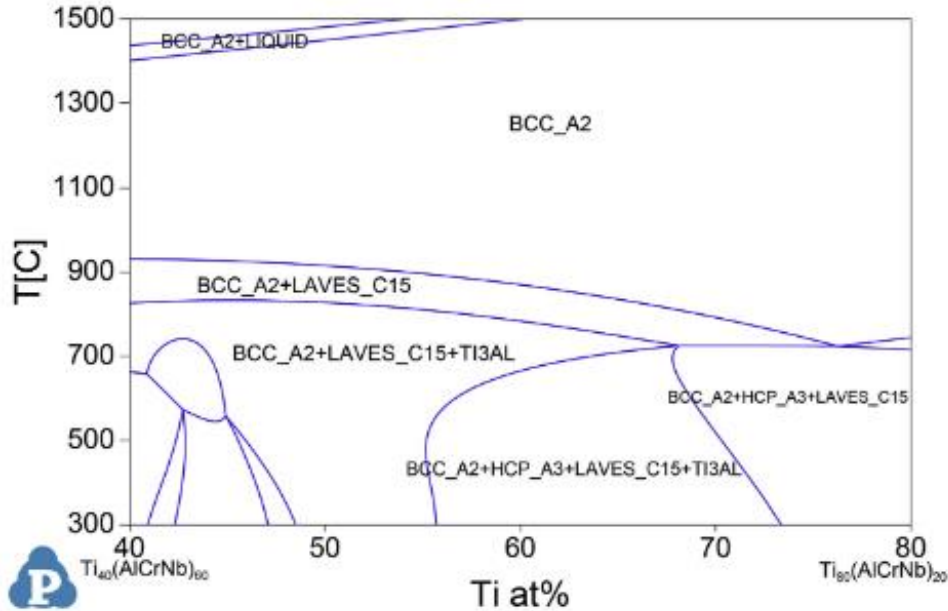
Figure 19: CALPHAD plot for $Ti_x(AlCrNb)_{100-x}$. Source: [21]

The mechanical properties of $Ti_{80}(AlCrNb)_{20}$ compare poorly with other β titanium alloys, regardless of ST [3]. The low stiffness values of the ST only samples are valuable in medical implants; however, the tradeoffs necessary to achieve this are undesirable. The low yield stress and lack of strain hardening make these alloys poor choices for implementation in the intended industries of aerospace and power generation. The addition of aging was predicted to increase the yield stress at a moderate cost to ductility by introducing α phase precipitates [2,54]. Instead, the sample was severely embrittled with premature fracture in the grip section.

3.3.2 Creep test results and discussion

Creep testing was performed at 85% and 90% of the yield stress which is 544 MPa and 576 MPa, respectively. First, a 12 hr ST sample and a 0.25 hr ST sample are tested at 85% yield stress. The creep plot for the 12 hr ST sample is shown in Figure 20. This test was ended prematurely due to equipment error,

so tertiary creep was not reached. The creep plot for the 0.25 hr ST sample is shown in Figure 21 and was halted after 250 hours without reaching tertiary creep.
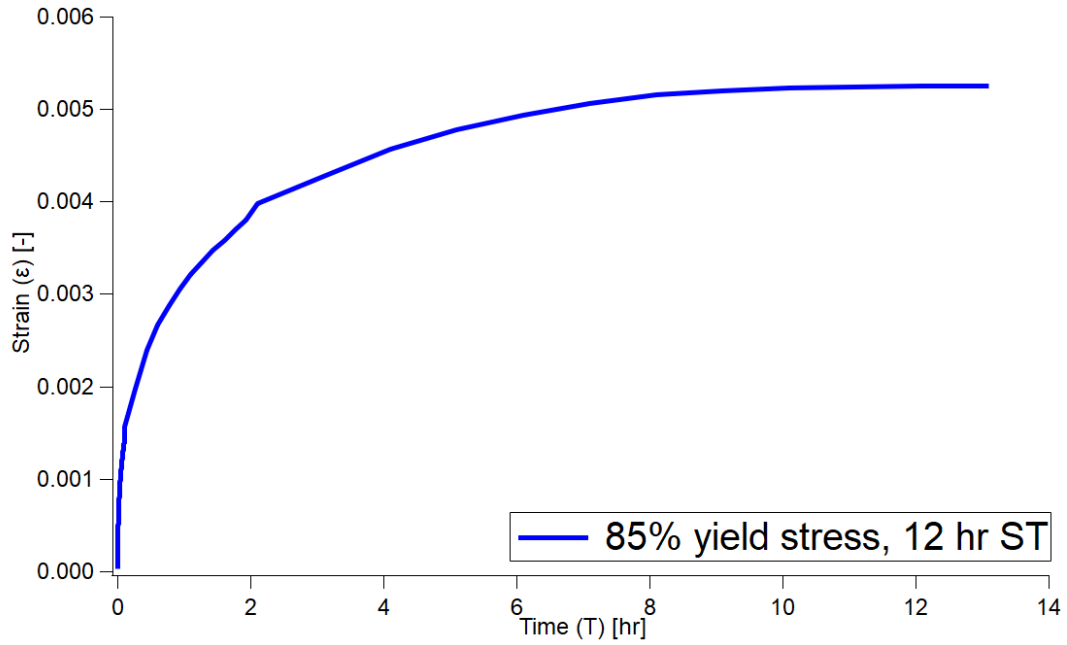
Figure 20: Creep test at 85% yield stress for 12 hr ST $Ti_{80}(AlCrNb)_{20}$
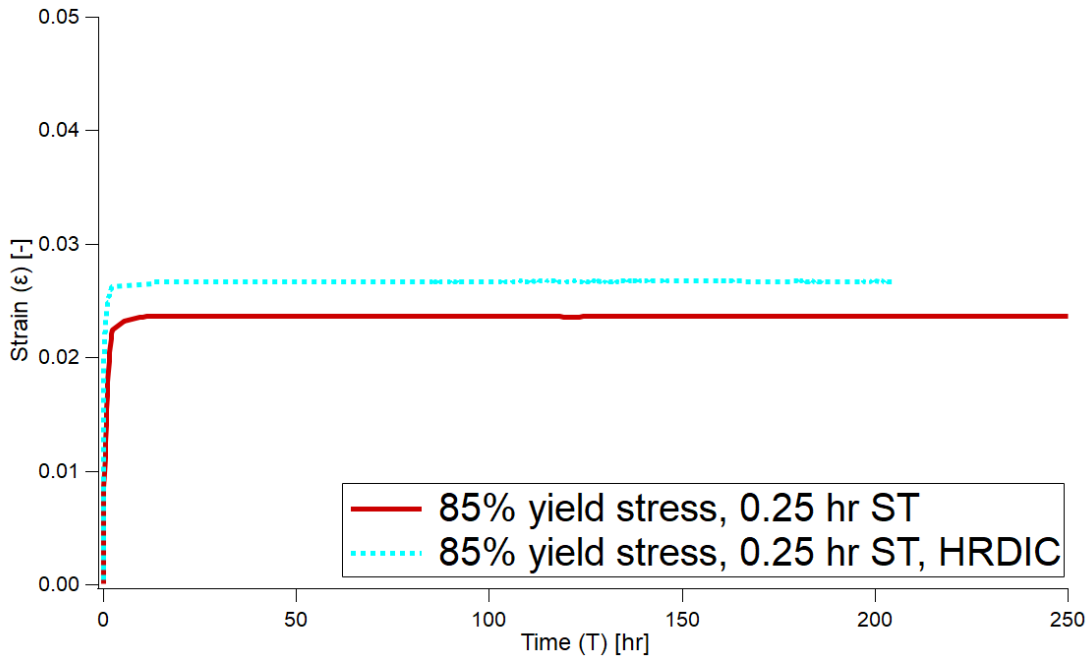
Figure 21: Creep tests at 85% yield stress for 0.25 hr ST $Ti_{80}(AlCrNb)_{20}$

Steady-state creep rates were measured as 9.2×10^{-7} s^{-1} for the 12 hr ST sample, 3.6×10^{-9} s^{-1} for the 0.25 hr ST sample, and 1.6×10^{-8} s^{-1} for the 0.25 hr ST sample for HRDIC. Primary creep times are 0.8 hr for the 12 hr ST sample, 5.3 hr for the 0.25 hr ST sample, and 1.9 hr for the 0.25 hr ST HRDIC enabled creep test. The 0.25 hr ST displayed a hardening effect entering secondary creep which reduced the steady-state strain rate. The non-HRDIC sample was held in creep for 12 days with no strain increase to indicate advancing to reaching tertiary creep. This is hypothesized to be due to a precipitation hardening effect from β to α phase stress induced transformation as stress induced transformations are a commonly observed phenomenon in metastable β titanium [32].

EBSD scans pre- and post-test were compared to confirm the presence of stress-induced α phases. There was no EBSD scan of the non-HRDIC sample pre-test, so a pre-test EBSD scan of another sample with the same 0.25 hr ST, shown in Figure 14, is used to compare against the post-test results. The post-test scan is shown in Figure 22.
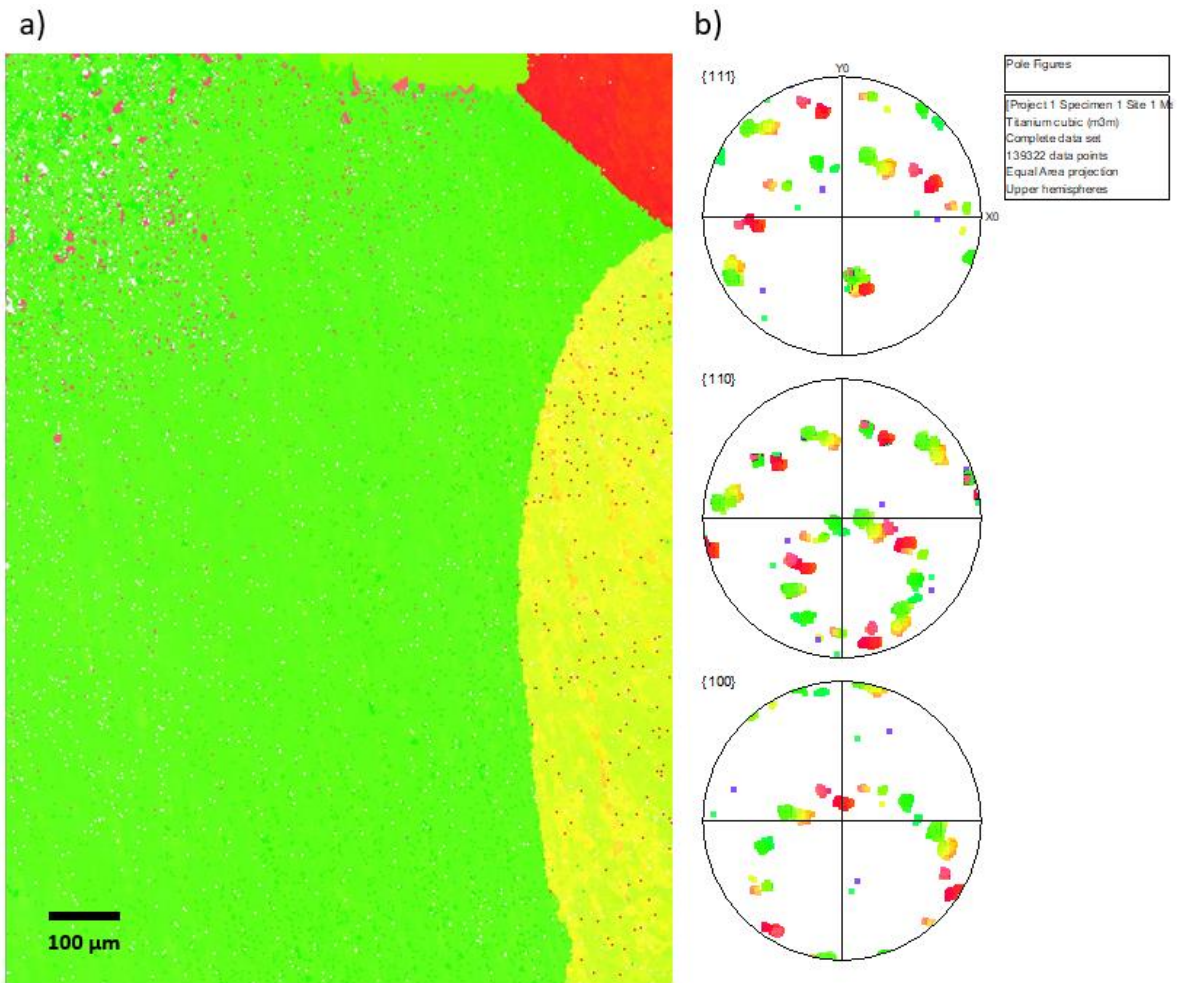
Figure 22: Post creep test EBSD of 0.25 hr ST sample a) EBSD scan b) Pole figure

To better compare the quantity and locations of precipitates, the data was stripped of BCC phases, so it

was just of the HCP phase, shown in Figure 23.
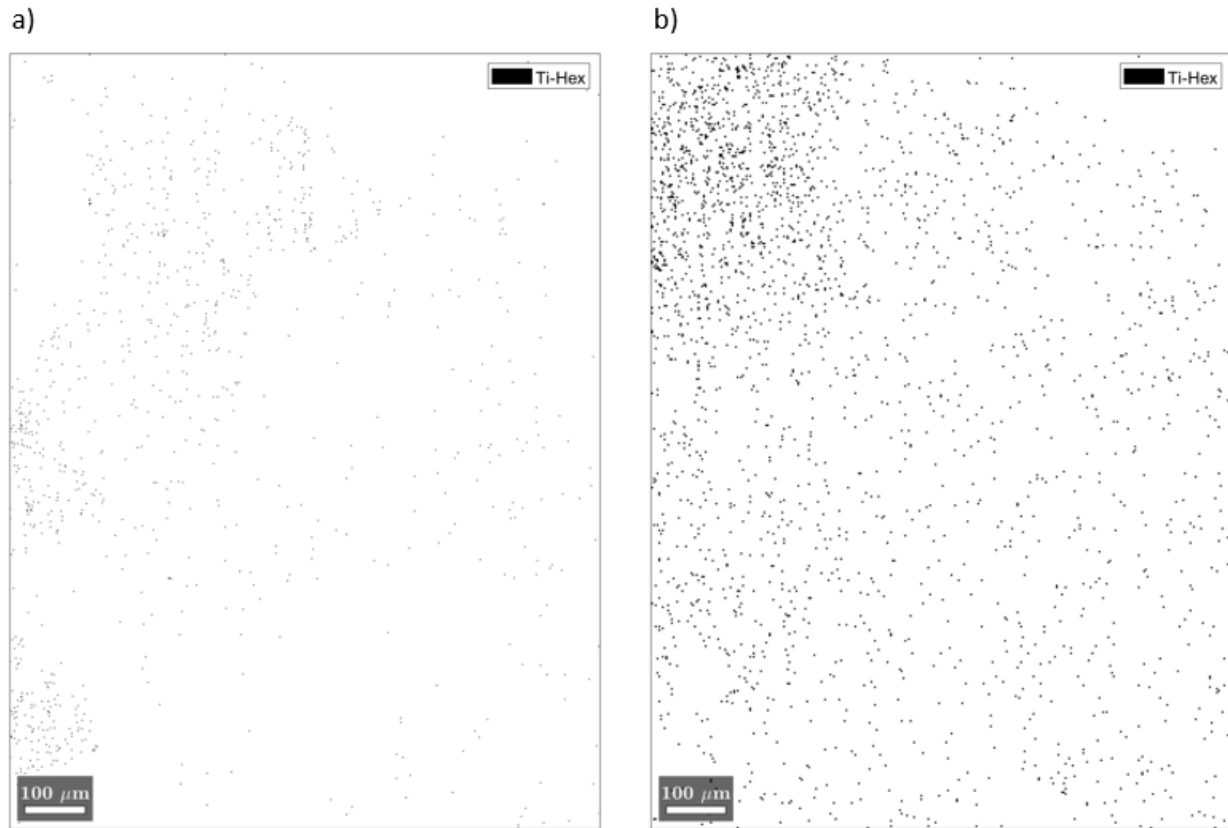
Figure 23: Phase plots from similar gage section locations of two samples with only HCP titanium a) Pre creep test phase plot b) Post creep test phase plot

HCP precipitates are confirmed in the post-test scan. HCP precipitates are known to be very small, sub-micron, so the size of the precipitation is in line with that [31,32]. The amount of precipitate in a 1001 x 1325 μm^2 field of view was measured as 2803 μm^2 which is 2.1% of the sample area. The precipitates were noted to be slightly larger at the grain boundaries than within the grains. This is shown in Figure 22 as the grain boundary at the top edge of the image has several larger precipitation sites than the smaller flecks of precipitates seen within the grains. HCP precipitates are unexpected as orthorhombic α''-martensite is the most common stress induced transformation.

As the 85% yield stress creep test stalled out in secondary creep, a 90% yield stress creep test was performed on a second 0.25 hr ST sample to compare the steady-state creep rates and the creep curve is plotted in Figure 24.

41
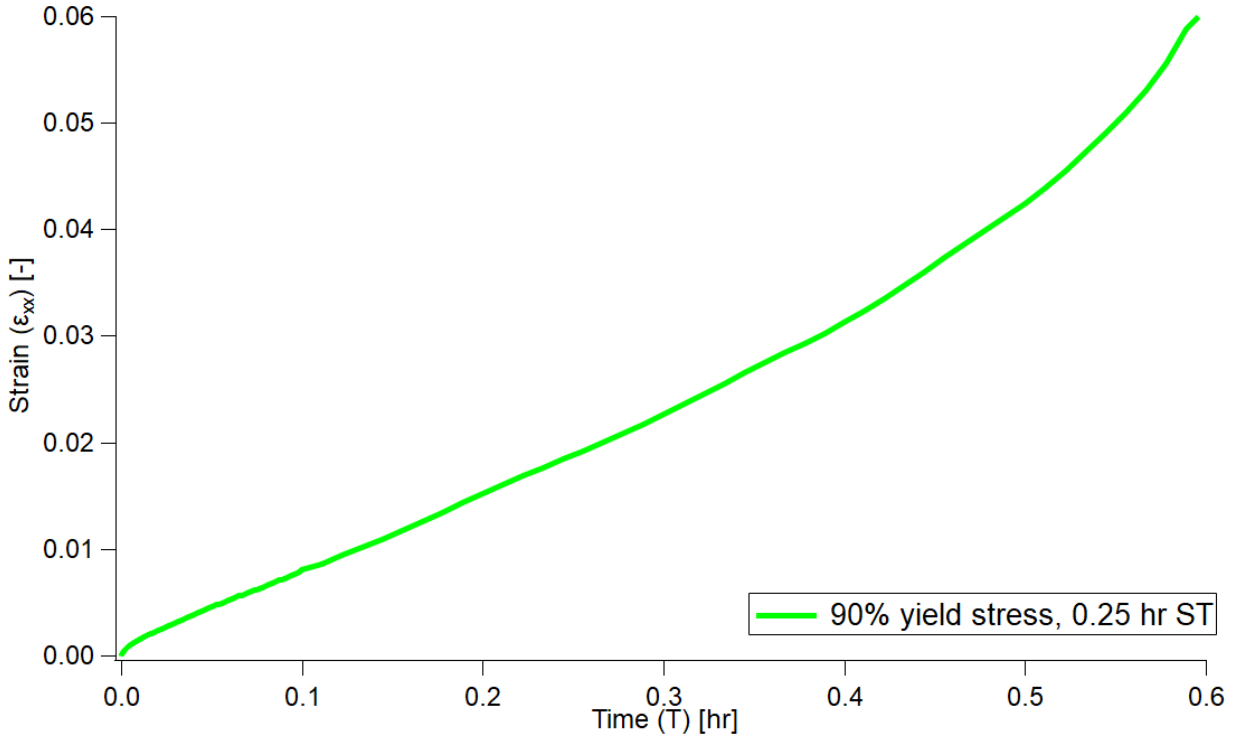
Figure 24: Creep test at 90% yield stress for 0.25 hr ST $Ti_{80}(AlCrNb)_{20}$

The steady-state strain rate was measured as 1.9×10^{-5} s^{-1}. The primary creep was extremely short at 0.023 hr for this creep test, and tertiary creep was measured at 0.233 hr with the expected accelerating strain rate until failure.

There were insufficient trials to correctly identify the creep exponents for $Ti_{80}(AlCrNb)_{20}$ with each specified ST. A preliminary approximation was made and calculated the creep exponent for $Ti_{80}(AlCrNb)_{20}$ with a 0.25 hr ST at 1100°C to be 124, which is extremely large and outside of other reported Ti-alloys [7,28,42,43].

The creep characterization revealed a creep exponent of 124 due to the steady-state creep rate being six orders of magnitude larger in the 90% yield stress creep test than the 85% yield stress creep test. The stress increase was only 32 MPa in the applied load. Titanium alloys have had large creep exponents reported [7,28,42,43] with the largest value being reported as 59 from Deguchi *et al.* [42], which was a

room temperature creep test on Ti-6Al-4V. The current value of 124 is over double the largest value reported for Ti-6Al-4V, thus a preliminary conclusion indicates that $Ti_{80}(AlCrNb)_{20}$ has exceptionally poor creep resistance. As the main objective of this thesis was to develop the Heaviside function based algorithm for measuring GBS, further characterization of $Ti_{80}(AlCrNb)_{20}$ is needed to fully understand its creep behavior, such as its creep exponents and other Arrhenius power law model parameters.

3.3.3 12 hr ST sample GBS analysis code results and discussion

Two creep tests were completed: one with a 12 hr ST sample and another with a 0.25 hr ST sample. These samples were both creep tested at 85% yield stress, 544 MPa, to compare the GBS between the ST for $Ti_{80}(AlCrNb)_{20}$. An as-cast sample was not tested for creep due to the significantly worse mechanical properties.

The first test was on a 12 hr ST $Ti_{80}(AlCrNb)_{20}$ sample. The EBSD scan with pole figures is shown in Figure 25.
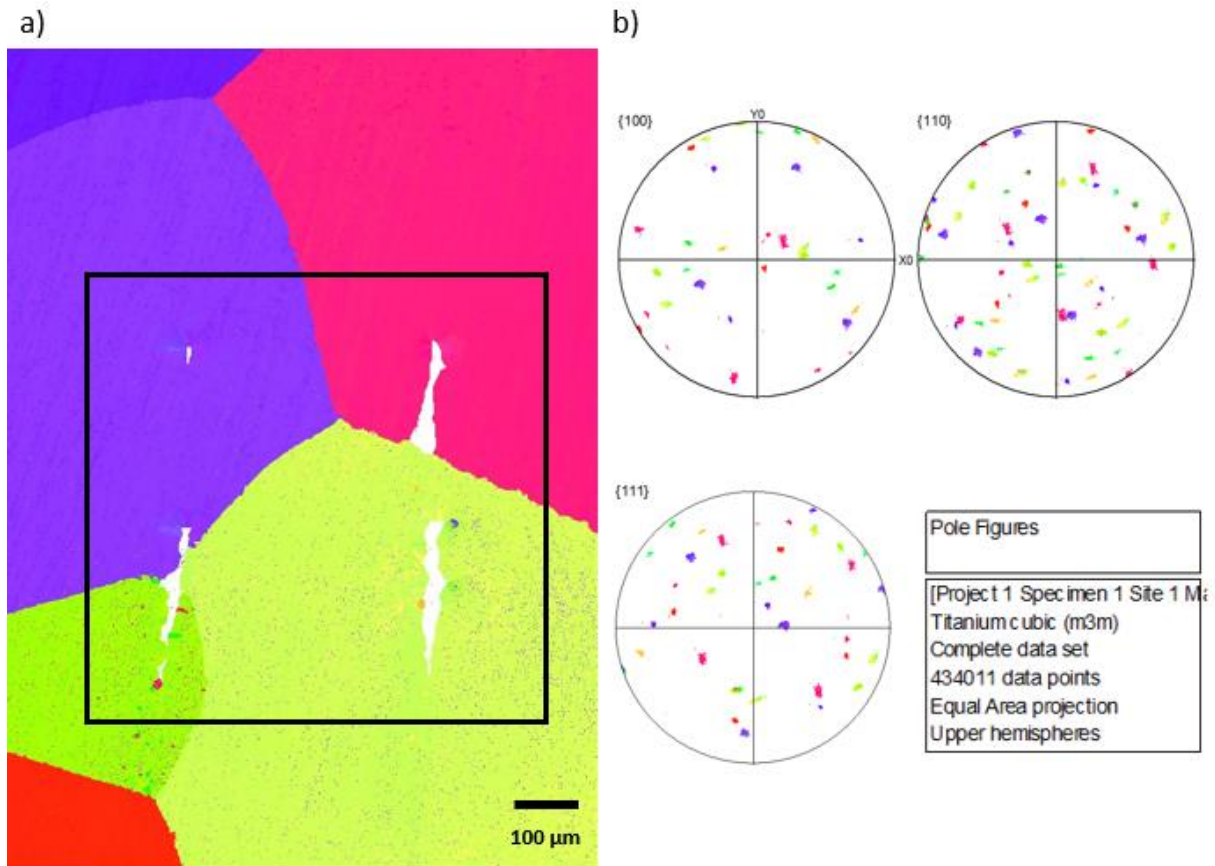
Figure 25: EBSD scan of 12 hr ST $Ti_{80}(AlCrNb)_{20}$ a) EBSD plot. Black box indicates area used in GBS analysis code b) Pole figures of EBSD plot

The fiducial markers for this test were placed with 300 µm spacing. Large streaks off the fiducial markers were observed which is due to excessive damage from polishing to remove the oxide layer prior to EBSD scans. This is corrected in the second test to reduce the polish time from 3 minutes to 15 seconds. The overlaid EBSD and HRDIC are shown in Figure 26.
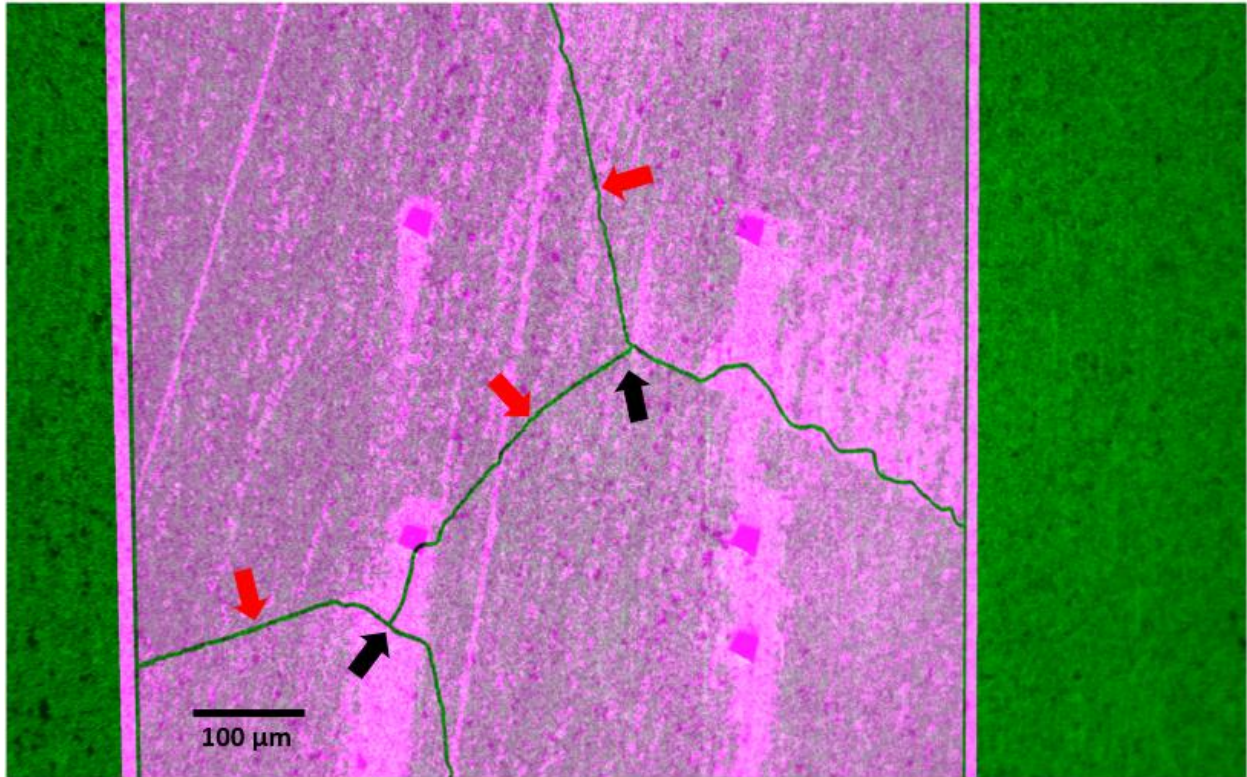
Figure 26: Overlaid EBSD and HRDIC images for 12 hr ST sample tested at 85% yield stress with green lines inside magenta region indicating grain boundaries. Red arrows also indicate grain boundaries, and black arrows indicate triple points

The important takeaway from Figure 26 is the grain boundary locations compared to the fiducial markers. Knowing the location of the grain boundaries reduces the uncertainty in separating which discontinuities were due to GBS and which were slip traces within the grain due to dislocation motion. The creep curve was previously reported in Section 3.3.2 Figure 20 with the sample reaching secondary creep before the test was prematurely ended. The calculated discontinuity map is shown in Figure 27.
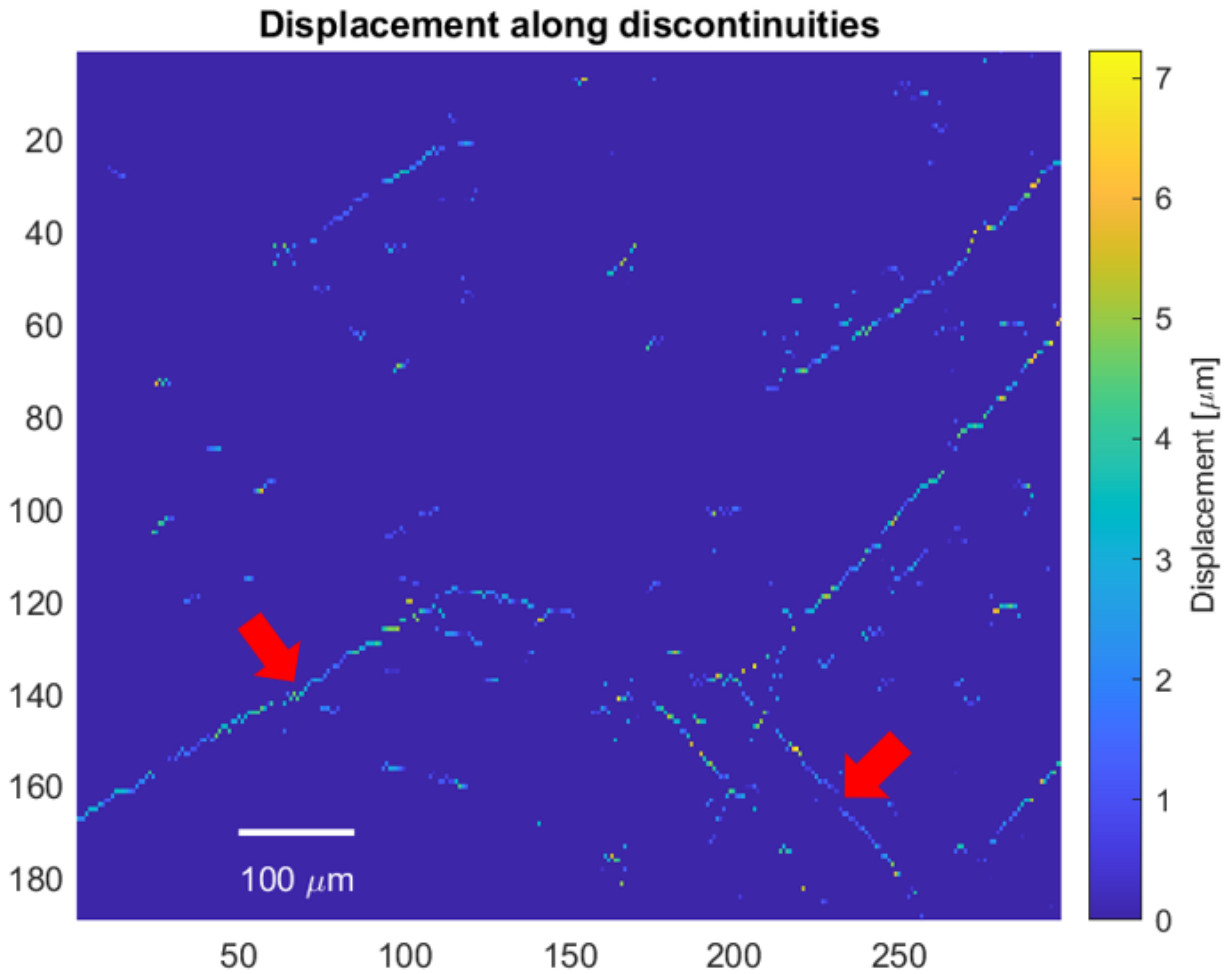
Figure 27: Map of discontinuities in 12 hr ST sample converted into the displacement of GBS or slip trace. Red arrows indicate active GBS grain boundaries

The average displacement between points on opposite sides of the discontinuities was measured to be 3 μm which means the magnitudes of both slip and GBS are approximately equal for 85% yield stress creep in the 12 hr ST sample. It is noted that this displacement is measured between points vertically across the discontinuities when the ideal measurement would be perpendicular across the discontinuity. This will be addressed in future versions of the analysis code to improve results. The discontinuities originating from 170 on the y-axis and 250 on the x-axis of Figure 27, indicated by red arrows, are both GBS sites. These are identified optically by comparison with Figure 26. These GBS sites are localized to single linear edges of the grains and do not continue around the entire grain boundary. Furthermore, the discontinuities for

the active GBS grain boundaries do not reach each other, so the triple junctions between three grains are not experiencing GBS. All other discontinuities are intragranular slip traces. The measured slip and GBS is not perfectly uniform along the observed discontinuities which is expected as these deformation mechanisms will vary in magnitude as they progress through the material. An additional contributing factor could be the discontinuity identification method used. Since the analysis code is built around identifying discontinuities via DIC marking the sigma value as -1, it is likely that points are being included and excluded incorrectly. If a point within the discontinuity is not marked as such, there is significant error introduced as points within the discontinuity have very large differences in displacements compared to the surrounding points. The opposite is true as well as points further away from the discontinuity will also be notably different. At this scale, small errors can result in noticeable error in the analysis code output as every pixel is equal to 0.58 μm for the microscope and camera setup. This is a flaw in the current GBS analysis code and will be addressed in future versions to improve measurement consistency.

These measurements were validated by using virtual extensometers in Vic-2D. By adding small, vertical extensometers that cross the discontinuities into the Vic-2D analysis, the code output for displacement across the discontinuity can be measured. These extensometers were placed vertically to match the x-y coordinate system in the DIC output and to match the data obtained from Heaviside function based GBS analysis code. The extensometer placements are shown in Figure 28.
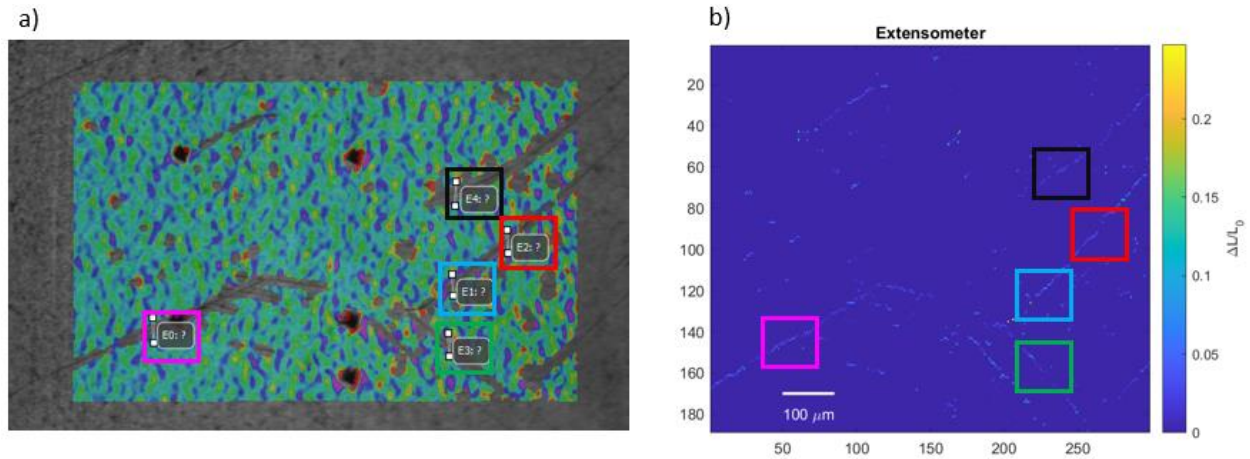
Figure 28: Extensometers for 12 hr ST sample a) Vic-2D extensometer placement in HRDIC image b) GBS analysis code extensometer output of $\Delta L/L_0$. Box color and locations matched between plots

The DIC extensometer outputs stay relatively small and consistent until the slip or GBS activates which occurs at the image number 175. After activation, there is a very clear jump in $\Delta L/L_0$ as the discontinuity grows. The outputs from the DIC extensometers are then compared against the GBS analysis code extensometer plot. The GBS analysis code is set to output what is essentially an extensometer placed at every point along each discontinuity that can be compared directly to the Vic-2D measurements. By taking the original length between the points directly above and below a discontinuity as reported in Section 3.2, Figure 17, the change in length between those two points was calculated. Dividing the change in length, ΔL, by the original length, L_0, results in an equivalent to the DIC extensometers that can be compared to validate that the code is properly identifying and quantifying the discontinuities. Table 4 shows the DIC extensometer outputs compared against the Heaviside function based GBS analysis code output for these extensometers.

Table 4: DIC extensometer and GBS analysis code extensometer comparisons for 12 hr ST sample

Color	E#	DIC extensometer ($\Delta L/L_0$)	GBS analysis code extensometer ($\Delta L/L_0$)
Pink	0	0.016	0.027
Cyan	1	0.019	0.016
Red	2	0.011	0.024
Green	3	0.008	0.009
Black	4	0.004	0.007

The GBS analysis code extensometer output has a minimum of 0.007 and a maximum of 0.027 $\Delta L/L_0$ which is again noted to be non-uniform along discontinuities with several hotspots observed with much larger values of 0.24. The DIC extensometer output has a minimum of 0.004 and a maximum of 0.019 $\Delta L/L_0$. It is noted that direct comparison of values at specific points is not possible as the DIC extensometers do not output indexes that could be used for comparison with GBS analysis code extensometers. The non-uniformity of measurements along discontinuities obfuscates comparisons, but optical inspection of Figure 28 and Table 4 report similar values for both DIC extensometers and GBS analysis code extensometers. Sections of discontinuities with larger $\Delta L/L_0$ values in the GBS analysis code also have larger values reported in the DIC extensometer. Furthermore, the DIC extensometers confirm a non-uniform displacement across a single discontinuity in Figure 28 and Table 4 with E1 and E2 reporting as 0.019 and 0.011, respectively. The largest error between measurements is 218% at E2 with 0.011 for DIC extensometer and 0.024 for GBS analysis code extensometer. At the scale utilized in this analysis, small fluctuations that could simply be the result of computation rounding or noise can result in a large error. A smaller step size than 5 and other computation changes may be required to reduce this error by refining the meshes utilized in DIC and GBS analysis code with the tradeoff of additional computational cost.

3.3.4 0.25 hr ST sample GBS analysis code results and discussion

The second crep test was on a 0.25 hr ST $Ti_{80}(AlCrNb)_{20}$ sample. The EBSD scan with pole figures was previously included in this thesis, shown in Section 3.1.4, Figure 14. The fiducial marker spacing was increased to 500 µm for this test to increase the area of analysis and potentially capture more GBS and slip for the analysis code. The creep curve is shown in Section 3.3.2, Figure 21 as the HRDIC enabled trace on the creep plot.

As stated in Section 3.3.2, the steady-state creep rate was measured to be 1.6 x 10^{-8} s^{-1}. Like the other test shown in Figure 21, this sample displays a hardening behavior going into secondary creep that reduces the steady-state creep rate significantly. The reduced final polishing to remove the oxide layer before EBSD resulted in minimal streaks around the fiducial markers; therefore, the correct overlaying of the EBSD and HRDIC was easier to verify and is shown in Figure 30.
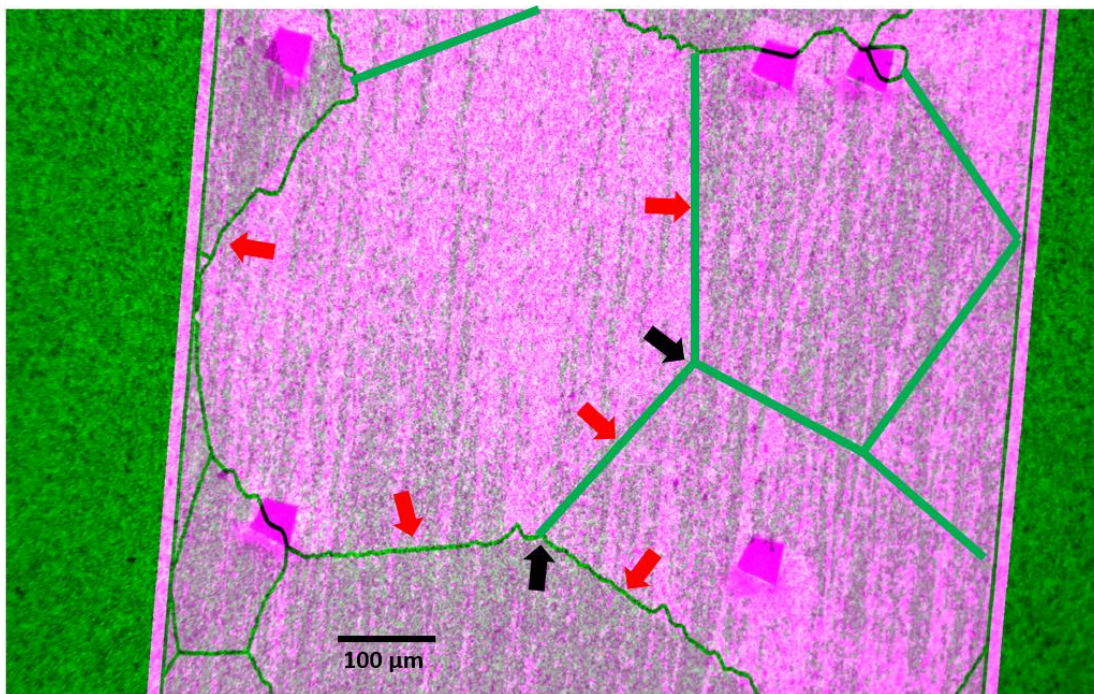
Figure 29: Overlaid EBSD and HRDIC image for 0.25 hr ST sample at 85% yield stress with grain boundaries marked via green lines in the magenta region. Red arrows are also indicating grain boundaries, and black arrows indicate triple points. Added green lines are due to large non-indexed regions preventing correct grain boundary identification

Due to the slip trace density of this sample, shown in Figure 31, the area analyzed with Vic-2D is limited as some of the surrounding areas have such a dense array of slip traces that the DIC algorithm utilized by Vic-2D was unable to correlate the displacements in these regions, even with increasing allowed error and allowing poorer pixel matches within subsets. Despite this, the reduced area still included several grain boundaries allowing for the quantification of any GBS. The discontinuity map is shown in Figure 32.
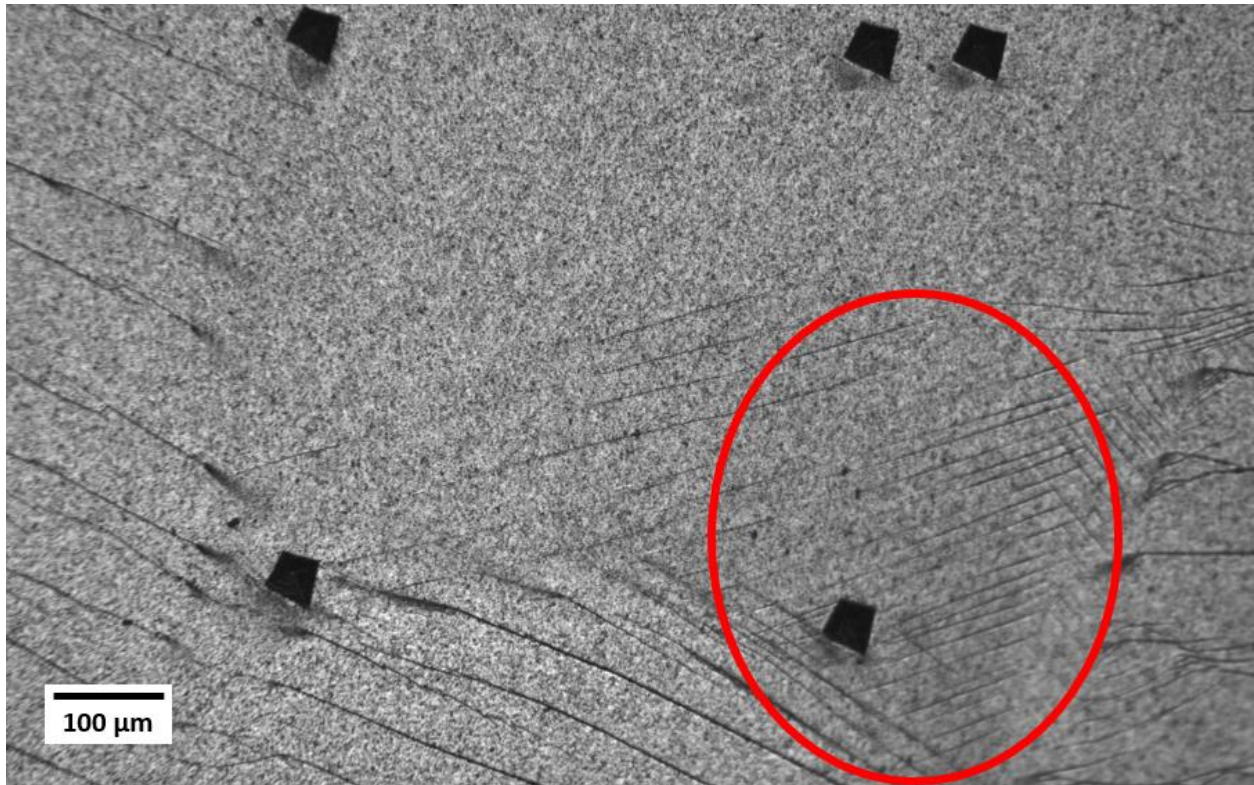
Figure 30: HRDIC image of 0.25 hr ST sample with the dense slip trace area within the fiducial markers circled
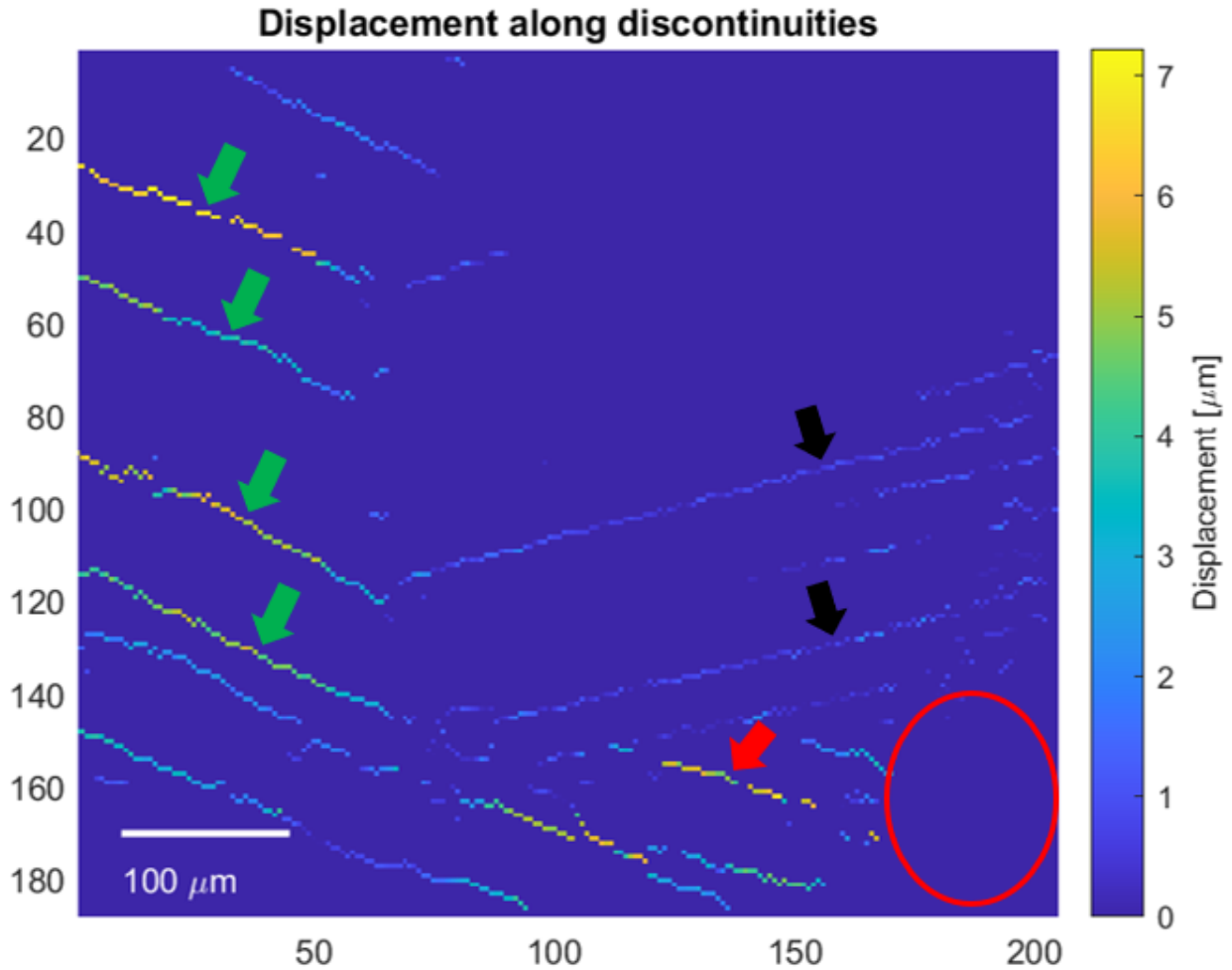
Figure 31: Displacement along grain boundaries and slip traces for the 0.25 hr ST sample tested at 85% yield stress in creep. Red arrows indicate GBS. Green arrows indicate slip traces terminating slip traces terminating against grain boundaries. Black arrows indicate slip traces passing through grain boundaries. Circled area is dense slip trace induced DIC failure

Differentiating between slip traces parallel to grain boundaries and GBS was difficult for this sample due to the number of discontinuities. By optically comparing the overlaid EBSD and HRDIC in Figure 30 to the GBS analysis code output in Figure 32, it appeared that there was GBS occurring in the lower right corner with one of the discontinuities originating between 150 and 200 on the x-axis marked with a red arrow in Figure 32. This area had some failure in the Vic-2D DIC correlation and is marked with a red circle, so confirmation of which discontinuity was GBS was unlikely. The slip traces originating along the left edge of Figure 32 are marked with green arrows and terminate at multiple grain boundaries with higher

misorientation angles of at least 40°. These slip traces have wider black streaks appear where they terminated against these grain boundaries. These are likely dislocations nucleating from the interior of the grain to the surface. The slip traces at 100-200 on the x-axis and 60-140 on the y-axis, marked with black arrows, appear to go directly through two grain boundaries which is unexpected as grain boundaries typically act as barriers to slip planes and is not seen anywhere else in the discontinuity data. The misorientation angle is much lower here at 5.5° and 7.0° which explains the slip trace being able to pass through this grain boundary as it is classified as a low angle grain boundary.

The slip traces captured showed varying magnitudes based on the grain they were observed in which was a different behavior from the 12 hr ST sample. The single site of GBS captured also showed a larger magnitude than the 12 hr ST sample. The discontinuities with larger displacements were measured at between 5 and 7 μm, which was approximately double the displacement measured in the 12 hr ST sample. Correlating this measurement to the global strain of both samples, this aligns with expected values as the global strain achieved by the 0.25 hr ST sample was 0.025 and the 12 hr ST sample reached 0.005, one fifth of the magnitude. The increase in slip activity correlated well to the larger global strains. Further, it was noted that there is variation in the magnitude of the slip activity in different regions of Figure 32 which correlated well to the different grains observed in the area. This means that the grain orientations are playing a role in the slip magnitude observed in these creep tests. The grains to the left of the fiducial markers have the largest measured slip at 7 μm across the discontinuity and are highly misoriented, at least 40°, from the grains at the center of the fiducial markers. As the grains inside the fiducial markers are all closely oriented with each other, they all report much lower slip magnitudes at 1 to 2 μm across the discontinuity with slip traces passing through the low angle grain boundaries. This shows the significant orientation dependence of the slip observed in $Ti_{80}(AlCrNb)_{20}$. These results were validated via comparing virtual extensometers from DIC and the GBS analysis code. The methodology was the same as

the methodology utilized in Section 3.3.3. DIC extensometers and GBS analysis code extensometers shown

in Figure 33. Table 5 compares the output values.
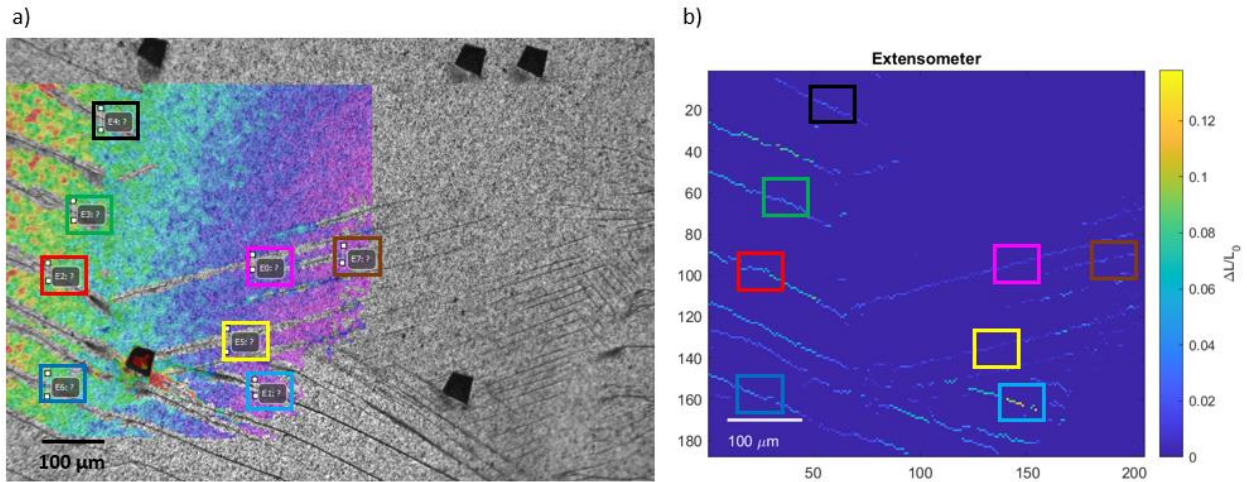
Figure 32: Extensometers for 0.25 hr ST sample a) Vic-2D extensometer placement in HRDIC image b) GBS analysis code extensometer output of $\Delta L/L_0$. Box color and locations matched between plots

Table 5: DIC extensometer and GBS analysis code extensometer comparisons for 0.25 hr ST sample

Color	E#	DIC extensometer ($\Delta L/L_0$)	GBS analysis code extensometer ($\Delta L/L_0$)
Pink	0	0.023	0.012
Cyan	1	0.056	0.093
Red	2	0.048	0.043
Green	3	0.022	0.024
Black	4	0.013	0.016
Yellow	5	0.014	0.013
Blue	6	0.020	0.022
Brown	7	0.015	0.021

Slip activates in E1 and E6 the earliest at around image 130; all other extensometers report slip activation

at approximately image 175. Same as in Section 3.3.3, the DIC extensometers report very little change in

length until there is a sudden, large increase in the length at the previous mentioned image numbers. The

slip traces marked by the black arrows in Figure 32 are E0, E5, and E7. The DIC extensometers have a minimum of 0.014 and maximum of 0.023, and the GBS analysis code extensometers have a minimum of 0.12 and maximum of 0.021. The slip traces marked by green arrows in Figure 32 are E2, E3, E4, and E6. The DIC extensometers have a minimum of 0.013 and maximum of 0.048, and the GBS analysis code extensometers have a minimum of 0.016 and maximum of 0.043. The GBS marked by red arrow in Figure 32 is E1. The DIC extensometer is 0.056, and the GBS analysis code extensometer is 0.093. The largest errors are 191% and 166% for E0 and E1, respectively. Overall, there is good agreement between the extensometer outputs, and the magnitudes of the extensometers match the trends of the displacement magnitudes. The discontinuities with the largest displacement magnitudes also have the largest extensometer magnitudes and vice versa for the smallest magnitudes. It is noted again that the magnitudes of extensometer outputs from the GBS analysis code along a single discontinuity can vary throughout the ranges listed which is once again likely due to the aforementioned reasons from Section 3.3.3.

Neither sample tested in creep exhibits significant GBS. The 12 hr ST sample exhibits more GBS than the 0.25 hr ST sample but only in number of active grain boundaries, not magnitude. The lack of GBS when it was expected to be the dominant deformation mechanism is likely due to the coarse grain size and lack of thermal activation. Larger grain sizes are known to be more resistant to GBS than smaller grains [45] and these samples were coarse grained with average grain sizes of 261 μm and 406 μm, with many assumed to be larger. With a sample gage section area of 4 mm x 2 mm, there were on average 16 grains across the width and 8 grains along the height with the assumed larger grains possibly reducing this even further in spots. At the sample surface, this equated to approximately 15 grain boundaries where slide can occur. When other damage mechanisms exist to accommodate dislocation motion, such as dislocation creep, GBS was no longer going to be the dominant deformation mechanism as $Ti_{80}(AlCrNb)_{20}$ was less resistant to these other creep deformation mechanisms [43]. The creep exponent of 124 supports this

further as, while it is extremely large, it still implies that dislocation creep is dominating [41]. The creep curves for all Ti$_{80}$(AlCrNb)$_{20}$ samples tested take the form of dislocation creep curves, especially glide creep, as the primary creep rate is much larger than the secondary creep rate. The large and plentiful slip traces observed in the 0.25 hr ST sample support this as the slip traces indicate dislocation glide. As the glide planes run into obstacles, such as grain boundaries, the dislocation motion is halted as there is no thermal energy added in room temperature creep to assist diffusion, specifically dislocation climb. Without an energetically favorable diffusion path, the dislocations become trapped and in tandem with the α phase precipitates observed, the creep rate is significantly reduced to the rates observed in the 85% yield stress creep tests in Section 3.3.2.

These observations and dominant deformation mechanism determination was due to the Heaviside function based GBS analysis code developed for this thesis. This tool was able to locate and quantify both GBS and slip traces based on continuous HRDIC data and a single microstructural map from EBSD. Comparisons between magnitudes of slip and GBS are possible which can then be related back to grain orientations to determine active slip systems, compare against Schmidt factors, and grain boundary misorientation influence on GBS and glide plane restriction. While the dominant deformation mechanism for Ti$_{80}$(AlCrNb)$_{20}$ in room temperature creep was not the expected GBS, the value of this tool made itself very apparent. The tool was able to identify that the expected deformation mechanism of GBS was not dominant, identify that dislocation creep is likely dominating, and find that the type of dislocation creep is likely to be glide creep without the need for additional testing or EBSD data.

Chapter 4. Conclusions

Ti$_{80}$(AlCrNb)$_{20}$ is the LMPEA tested in this thesis to characterize its mechanical properties, creep resistance, and localized slip damage mechanisms in creep, such as GBS. Ti$_{80}$(AlCrNb)$_{20}$ is tested with both 12 hr ST and 0.25 hr ST at 1100°C to compare mechanical properties and steady-state creep rates prior to GBS

measurement. It is found that the literature recommended 0.25 hr ST at 1100°C is confirmed to produce significantly improved ductility in $Ti_{80}(AlCrNb)_{20}$ in tensile tests. Additionally, the 0.25 hr ST at 1100°C prevented the already coarse grain size of 261 μm from growing any larger as well as allowing precipitate hardening to occur during creep testing at 85% yield stress, 544 MPa.

This thesis presents a method for measuring GBS and localized slip which was used on $Ti_{80}(AlCrNb)_{20}$ to measure GBS during creep testing as it is expected to be the dominant damage mechanism for β titanium. This analysis code is proven to be able to locate and measure displacements across discontinuities from the output of a commercial DIC software package, Vic-2D. The GBS is found to be minimal at both ST in room temperature creep at 85% yield stress. This matches the very large creep exponent measured as the creep exponent implies that dislocation creep is dominating. By examining the output of the Heaviside function based GBS analysis code, the GBS is confirmed to minimal at both ST, especially in the 0.25 hr ST sample. The magnitude, quantity, and orientations of the slip traces observed in the 0.25 hr ST sample indicate that glide creep is dominating as the slip traces are consistent within each grain, so there is at least one slip system being activated that edge dislocations are traveling on. This increased slip activity correlates to a larger global strain for the creep tests with 0.25 hr ST samples. As the quantity and magnitude of slip traces align with the global strain, this is further confirmation that the GBS analysis code is functioning correctly and is a useful tool for examining microstructure damage.

This analysis code has potential to be a useful tool in future material development and testing as continuous microstructure damage tracking at this scale is a new capability. Linking specific damage types and magnitudes to microstructure features and global behavior is important to fully understanding material behavior in many environments. Further, removing the need for interruptions during material testing will produce improved results for researchers by removing any unwanted effects, such as thermic cycling. It will prove invaluable in the future creep testing performed on $Ti_{80}(AlCrNb)_{20}$ as pure creep tests

at elevated temperatures will be possible with informative analysis on the microstructure damage mechanisms to aid in determining, verifying, and quantifying dominant creep mechanisms.

Chapter 5. Future Work

The first feature addition to the GBS analysis code will be to calculate Schmidt factors to predict yield in each grain based on orientation. This can be verified against the HRDIC data by observing which grains yield first and if it agrees with the Schmidt factor analysis. Furthermore, the observed slip traces can be compared against the crystal orientation to determine active slip systems. This can be can also be used to verify the slip trace versus GBS identification that is currently only being done optically.

The GBS analysis code is currently unable to account for small errors in the DIC output. For example, if there is a point in the middle of a larger discontinuity that is not marked as discontinuous, that point will cause a split in the discontinuity and obfuscate the analysis. Another example of this is discontinuities at the edge of the selected analysis region in Vic-2D. The analysis code current treats these as whole discontinuities, but this is often inaccurate. These discontinuities also cause issues in the discontinuity quantification as the outside edge of the discontinuity is treated as if it is in the bulk crystal which is very inaccurate and leads to extremely large magnitudes of GBS being measured incorrectly.

The scanning technique to find and index the discontinuities also needs some additional work. Currently, the discontinuities are identified by scanning down columns which will cause errors if the discontinuities are fully vertical or near vertical. Future iterations of this code will combine a column- and row-based scan to increase reliability and accuracy of discontinuity identification and measurement. The scanning technique will be further improved to identify the edges of the discontinuity as perpendicular to the discontinuity direction as this will provide a more accurate measurement of the discontinuity than using two points that are in line with each other vertically. With improvement of the scanning technique, the continuity of the scanned in discontinuities should be improved in future iterations of the GBS analysis

code as the current code output can appear jagged and be discontinuous along discontinuities with missing pixels breaking up longer discontinuities. Without continuous discontinuities, it will be significantly more difficult to automate GBS and slip trace measurement in the future. Furthermore, the scanning methodology detects many smaller discontinuities that are unnecessary for slip trace and GBS measurement, and they only serve to create noise in the discontinuity measurements plots and data. Future versions of this code will introduce thresholding to remove these from the data.

$Ti_{80}(AlCrNb)_{20}$ was originally selected as the material for this thesis due to its promising mechanical properties [21]. However, it became clear early in the testing that the samples of $Ti_{80}(AlCrNb)_{20}$ utilized in this thesis had poor tensile behavior. Density-functional theory (DFT) based simulations are currently underway to computationally determine the theoretical mechanical behavior of $Ti_{80}(AlCrNb)_{20}$. A possible explanation for the poor experimental tensile behavior could be the large average grain size and even larger grains present in the samples that covered almost the entire gage section. Grains on this scale could explain the low yield stress and lack of strain hardening. To confirm this, thermo-mechanical processing is needed to break down the large grains present in the stock material and recrystallize them into much smaller β phase grains. This material would then need to repeat all testing to confirm that was indeed the detrimental factor. Additionally, there may be more optimal ST and aging treatments as super beta transus heat treatments are typically only 20 to 30°C greater than the beta transus [2,54], and aging treatments have many different variations including duplex aging, temperature range, time frame, and cooling. There will be an aging treatment that does not embrittle the alloy as observed in this thesis.

The measured creep exponent of 0.25 hr ST $Ti_{80}(AlCrNb)_{20}$ was very large and does not correspond to a known deformation mechanism. Further creep testing will shed light on this, especially at elevated temperature creep testing. As Arrhenius law is not designed for room temperature creep due to the total lack of thermal activation, the creep exponent should be reduced to a more reasonable level in elevated

temperature creep that can be used to properly model creep behavior. An optimal ST for creep behavior will be found as well to maximize creep resistance for these tests.

Chapter 6. References

1. D. Sinan Körpe, M. Gilani, and D. Sinan KÖRPE, *Airline Weight Reduction to Minimize Direct Operating Cost* (2019).

2. R. P. Kolli and A. Devaraj, Metals (Basel) (2018).

3. M. Niinomi, *Mechanical Properties of Biomedical Titanium Alloys* (1998).

4. H. Agripa and I. Botef, in *Titanium Alloys - Novel Aspects of Their Manufacturing and Processing [Working Title]* (IntechOpen, 2019).

5. M. J. R. Barboza, C. Moura Neto, and C. R. M. Silva, Materials Science and Engineering A (2004).

6. J. F. Xiao, X. K. Shang, Y. Li, Q. W. Guan, and B. He, Materials Science and Technology **38**, 469 (2022).

7. L. Badea, M. Surand, J. Ruau, and B. Viguier, UPB Scientific Bulletin, Series B: Chemistry and Materials Science (2014).

8. S. W. Xin, Y. Q. Zhao, Y. F. Lu, Q. Li, and H. Y. Yang, Materials Science and Engineering A (2013).

9. S. K. Sahay, S. K. Singh, and A. K. Ray, National Institute of Technology (2005).

10. J. F. Xiao, X. K. Shang, J. H. Hou, Y. Li, and B. B. He, International Journal of Plasticity **146**, (2021).

11. O. N. Senkov, J. D. Miller, D. B. Miracle, and C. Woodward, Nature Communications **6**, (2015).

12. J. Carter and M. Mills, *Exploration of Local Strain Accumulation in Nickel-Based Superalloys* (2012).

13. H. Li, X. Liu, Q. Sun, L. Ye, and X. Zhang, MDPI (2020).

14. M. A. Linne, A. Venkataraman, M. D. Sangid, and S. Daly, Experimental Mechanics **59**, 643 (2019).

15. M. A. Linne, T. R. Bieler, and S. Daly, International Journal of Plasticity (2020).

16. S. v. Bobylev, A. K. Mukherjee, I. A. Ovid'Ko, and A. G. Sheinerman, International Journal of Plasticity **26**, 1629 (2010).

17. B. Cantor, I. T. H. Chang, P. Knight, and A. J. B. Vincent, Materials Science and Engineering A **375–377**, 213 (2004).

18. B. S. Murty, J. W. Yeh, and S. Ranganathan, in *High Entropy Alloys* (Elsevier, 2014), pp. 1–12.

19. Y. Zhang, in *High-Entropy Materials* (Springer Singapore, 2019), pp. 1–33.

20. J. W. Yeh, S. K. Chen, S. J. Lin, J. Y. Gan, T. S. Chin, T. T. Shun, C. H. Tsau, and S. Y. Chang, Advanced Engineering Materials **6**, 299 (2004).

21. Y. C. Liao, T. H. Li, P. H. Tsai, J. S. C. Jang, K. C. Hsieh, C. Y. Chen, J. C. Huang, H. J. Wu, Y. C. Lo, C. W. Huang, and I. Y. Tsao, Intermetallics (Barking) (2020).

22. F. Kies, X. Wu, B. Hallstedt, Z. Li, and C. Haase, Materials and Design **198**, (2021).

23. K. K. Tseng, Y. C. Yang, C. C. Juan, T. S. Chin, C. W. Tsai, and J. W. Yeh, Science China Technological Sciences (2018).

24. Y. D. Wu, Y. H. Cai, X. H. Chen, T. Wang, J. J. Si, L. Wang, Y. D. Wang, and X. D. Hui, Materials and Design (2015).

25. E. P. George, W. A. Curtin, and C. C. Tasan, Acta Materialia **188**, 435 (2020).

26. H. Warlimont, in *Springer Handbooks* (Springer, 2018), pp. 195–206.

27. ASM International (n.d.).

28. M. J. R. Barboza, E. A. C. Perez, M. M. Medeiros, D. A. P. Reis, M. C. A. Nono, F. P. Neto, and C. R. M. Silva, Materials Science and Engineering A (2006).

29. R. Sahoo, B. B. Jha, and T. K. Sahoo, Transactions of the Indian Institute of Metals (2018).

30. Titanium '99: Science and Technology 56 (1999).

31. Z. Zhang, T. Wang, J. Han, Z. Ren, R. Wu, and J. Sun, Materials Letters **250**, 46 (2019).

32. M. H. Cai, C. Y. Lee, S. Kang, and Y. K. Lee, Scripta Materialia **64**, 1098 (2011).

33. C. Smith, (n.d.).

34. A. Orozco-Caballero, F. Li, D. Esqué-de los Ojos, M. D. Atkinson, and J. Quinta da Fonseca, Acta Materialia **149**, 1 (2018).

35. D. Yang, W. Tian, X. Zhang, K. Si, and J. Li, Frontiers in Materials **8**, (2021).

36. M. Kassner, *Fundamentals of Creep in Metals and Alloys*, Third (Elsevier, 2015).

37. W. Soboyejo, *Mechanical Properties of Engineered Materials* (New York : Marcel Dekker, 2003).

38. C. R. Weinberger, B. L. Boyce, and C. C. Battaile, International Materials Reviews **58**, 296 (2013).

39. J. Kumar, S. G. S. Raman, and V. Kumar, Transactions of the Indian Institute of Metals (2016).

40. J. Yanagimoto, in *CIRP Encyclopedia of Production Engineering* (Springer Berlin Heidelberg, Berlin, Heidelberg, 2016), pp. 1–7.

41. R. W. Hertzberg and H. Saunders, Journal of Pressure Vessel Technology **107**, (1985).

42. M. Deguchi, S. Yamasaki, M. Mitsuhara, H. Nakashima, and Y. Ota, Keikinzoku/Journal of Japan Institute of Light Metals **70**, 405 (2020).

43. R. Dutton, (1996).

44. S. Hémery, C. Tromas, and P. Villechaise, Materialia (Oxf) **5**, 100189 (2019).

45. R. L. Bell and T. G. Langdon, Journal of Materials Science **2**, 313 (1967).

46. M. J. Donachie and S. James. Donachie, *Superalloys : A Technical Guide* (ASM International, 2002).

47. G. J. Pataky, H. Sehitoglu, and H. J. Maier, Journal of Nuclear Materials **443**, 484 (2013).

48. S. I. A. Jalali, P. Kumar, and V. Jayaram, JOM **72**, 4522 (2020).

49. (n.d.).

50. G. J. Pataky and H. Sehitoglu, Experimental Mechanics **55**, 53 (2015).

51. A. D. Kammers and S. Daly, Experimental Mechanics **53**, 1743 (2013).

52. J. C. Stinville, M. A. Charpagne, F. Bourdin, P. G. Callahan, Z. Chen, M. P. Echlin, D. Texier, J. Cormier, P. Villechaise, T. M. Pollock, and V. Valle, Materials Characterization **169**, (2020).

53. F. Bourdin, J. C. Stinville, M. P. Echlin, P. G. Callahan, W. C. Lenthe, C. J. Torbet, D. Texier, F. Bridier, J. Cormier, P. Villechaise, T. M. Pollock, and V. Valle, Acta Materialia **157**, 307 (2018).

54. S. Rajan Soundararajan, J. Vishnu, G. Manivasagam, and N. Rao Muktinutalapati, in *Welding - Modern Topics* (IntechOpen, 2021).

55. P. H. Lin, J. C. Huang, X. K. Zhang, H. S. Chou, W. S. Chuang, T. Y. Liu, Y. C. Liao, and J. S. C. Jang, Materials Science and Engineering: A 140140 (2020).

56. F. Bachmann, R. Hielscher, and H. Schaeben, Ultramicroscopy **111**, 1720 (2011).

57. R. Bigger, B. Blaysat, C. Boo, M. Grewer, J. Hu, A. Jones, M. Klein, K. Raghavan, P. Reu, T. Schmidt, T. Siebert, M. Simenson, D. Turner, A. Vieira, and T. Weikert, *A Good Practices Guide for Digital Image Correlation* (2018).

Appendices

Appendix A. EBSD and HRDIC overlay code

```
close all
clear
clc
```

Import Script for EBSD Data

This script was automatically created by the import wizard. You should run the whoole script or parts of

it in order to import your data. There is no problem in making any changes to this script.

Specify Crystal and Specimen Symmetries

```
% crystal symmetry
CS = {...
  'notIndexed',...
  crystalSymmetry('6/mmm', [3 3 4.7], 'X||a*', 'Y||b', 'Z||c*', 'mineral', 'Ti-Hex', 'color',
[0.53 0.81 0.98]),...
  crystalSymmetry('m-3m', [3.2 3.2 3.2], 'mineral', 'Titanium cubic', 'color', [0.56 0.74
0.56])};

% plotting convention
setMTEXpref('xAxisDirection','north');
setMTEXpref('zAxisDirection','outOfPlane');
```

Specify File Names

```
% path to files
pname = 'F:\Lab Data\EBSD\06-15-22-Ti80 #16\Ti-80 #16 06152022 Specimen 1 Site 1 Map Data 1';

% which files to be imported
fname = [pname '\Ti-80 #16 06152022 Specimen 1 Site 1 Map Data 1.cpr'];
```

Import the Data

```
% create an EBSD variable containing the data
ebsd = EBSD.load(fname,CS,'interface','crc',...
  'convertEuler2SpatialReferenceFrame');

% all code above from MTEX import wizard
```

Grain Reconstruction (cleanup non indexed and Ti Hex data)

```matlab
[grains,ebsd.grainId,ebsd.mis2mean]=calcGrains(ebsd); %calculate grains

notIndexed=grains('notIndexed'); %index notIndexed grains
toRemove1=notIndexed(notIndexed.grainSize ./ notIndexed.boundarySize<1.2); %index notIndexed
grains unlikely to be actual grains
ebsd(toRemove1)=[]; %remove from ebsd data

[grains,ebsd.grainId,ebsd.mis2mean]=calcGrains(ebsd); %calculate grains
TiHex=grains('Ti-Hex'); %index HCP grains
toRemove2=TiHex(TiHex.grainSize ./ TiHex.boundarySize<1.2); %index HCP grains unlikely to be
actual grains
ebsd(toRemove2)=[]; %remove from ebsd data
```

Calculate and plot clean grain boundaries

```matlab
[grains,ebsd.grainId,ebsd.mis2mean]=calcGrains(ebsd); %calculate grains
ebsd(grains(grains.grainSize<=5))=[]; %remove all grains below specified size
[grains,ebsd.grainId,ebsd.mis2mean]=calcGrains(ebsd('indexed')); %calculate grains of indexed
data
grains=smooth(grains,4); %smooth grain boundaries
gB=grains.boundary; %save grain boundaries

cd 'F:\Lab Data\EBSD\06-15-22-Ti80 #16' %change directory to location of EBSD data

figure %plot EBSD with grain boundaries
plot(ebsd)
hold on
plot(gB,'linewidth',2)
saveas(gcf,'EBSD_cleaned.tif') %save .tif
EBSD_cleaned=imread('EBSD_cleaned.tif'); %read image back in
figure
imagesc(EBSD_cleaned) %plot it again as an image
[xEBSD,yEBSD]=ginput; %select fiducial markers
EBSDmark=[xEBSD yEBSD]; %make one variable
```

Misorientation

```matlab
gB_TC=gB('Titanium cubic','Titanium cubic'); %locate grain boundaries between BCC grains
figure
plot(gB_TC,gB_TC.misorientation.angle./degree,'linewidth',4) %calculate and plot misorientation
mtexColorbar('title','misorientation angle (degree)') %make colorbar for misorientation angle
saveas(gcf,'Grain Misorientation.tif') %save image
```

Import reference HRDIC image

```
cd 'F:\Lab Data\Ti80(AlCrNb)20 Creep\06-26-22 Ti80 #16 HRDIC Creep (partial)' %change directory
to HRDIC data

HRDIC=imread('06-26-22 Ti80 #16 HRDIC Creep-0025_0.tif'); %read in reference image
figure
imagesc(HRDIC) %plot ref image
[xHRDIC,yHRDIC]=ginput; %select fiducial markers
DICmark=[xHRDIC yHRDIC]; %change to one variable
```

Warp EBSD to HRDIC image

```
cd 'F:\Lab Data\EBSD\06-15-22-Ti80 #16' %change directory back to EBSD data

tform=fitgeotrans(EBSDmark,DICmark,'projective'); %find transform to align fiducial markers
Jregistered=imwarp(EBSD_cleaned,tform,'OutputView',imref2d(size(HRDIC))); %apply transform to
EBSD and plot on top of reference HRDIC image
figure
imshowpair(HRDIC,Jregistered) %plot overlaid image

saveas(gcf,'Final overlay.tif') %save overlaid image
```

[Published with MATLAB® R2020b](#)

Appendix B. Heaviside function based GBS analysis code

```
% Heaviside function

close all
clear
clc
```

Read in DIC images

```
cd 'F:\Lab Data\Ti80(AlCrNb)20 Creep\06-26-22 Ti80 #16 HRDIC Creep (partial)\Vic-2D subset size
25' %select directory with Vic-2D output data

S=dir('*.mat');  %Save all directory info for files .mat file extension
N=numel(S);      %Count # of .mat files

for k=1:N
    C(k)=load(S(k).name);  %Read in image data and save each to index in structure
end
```

Measure and plot difference of discontinuities vs bulk

```matlab
SubsetSize1=51; %length of subset sides in pixels, must be odd number

DistPerPixel=0.5787; %microns per pixel in microscope

for i=1:N %loop through all images
    [row,col]=find(C(i).sigma==-1); %index all points with high uncertainty
    [rowZero,colZero]=size(C(i).u); %size of all future data maps
    uDisc=zeros(rowZero,colZero); %presize matrix
    for j=1:length(row) %loop through all indexes
        rowIndex=row(j)-((SubsetSize1-1)/2):row(j)+((SubsetSize1-1)/2); %create row&col indexes
around discontinuity
        colIndex=col(j)-((SubsetSize1-1)/2):col(j)+((SubsetSize1-1)/2);
        if max(rowIndex)>rowZero||max(colIndex)>colZero||min(rowIndex)<1||min(colIndex)<1 %reduce
size of subset if it exceeds data matrix
            rowTooLong=find(rowIndex>rowZero);
            rowIndex(rowTooLong)=[];
            colIndex(rowTooLong)=[];

            colTooLong=find(colIndex>colZero);
            rowIndex(colTooLong)=[];
            colIndex(colTooLong)=[];

            rowTooShort=find(rowIndex<1);
            rowIndex(rowTooShort)=[];
            colIndex(rowTooShort)=[];

            colTooShort=find(colIndex<1);
            rowIndex(colTooShort)=[];
            colIndex(colTooShort)=[];
        end
        temp=C(i).u; %extract u matrix
        tempSubset=temp(rowIndex,colIndex); %extract all u within subset
        tempSubsetAvg=mean(tempSubset,'all'); %average the u values within subset
        tempSubsetDifFromAvg=tempSubsetAvg-temp(row(j),col(j)); %difference between average and
value at discontinuity
        uDisc(row(j),col(j))=tempSubsetDifFromAvg; %write u discontinuity
    end
    C(i).uDisc=uDisc; %write to structure
end

t=tiledlayout(2,2,'TileSpacing','Compact'); %plotting setup for 2x2 figure
hold on
title(t,'Plots of DIC data')
xlabel(t,'x position (pixels)')
ylabel(t,'y position (pixels)')
nexttile(1)
title('sigma')
nexttile(2)
title('uDisc')
nexttile(3)
```

```matlab
title('exx')
nexttile(4)
title('u')
set(gca,'ydir','reverse')
for i=1:N %loop through all images and plot to figure
    nexttile(1)
    imagesc(C(i).sigma)
    nexttile(2)
    imagesc(C(i).uDisc)
    nexttile(3)
    imagesc(C(i).exx)
    nexttile(4)
    imagesc(C(i).u)
    pause(0.02)
end

nexttile(1) %select tile in figure
hold on
axis([1 colZero 1 rowZero]) %set axes
c=colorbar;
c.Label.String='sigma [pixels]'; %create and label colorbar
plot([50;(50+(175/5))],[165;165],'-k','LineWidth',2) %plot scale bar
text(50,175,'100 \mum','HorizontalAlignment','left') %plot text for scale bar
title('sigma')

nexttile(2) %repeated from above
hold on
axis([1 colZero 1 rowZero])
c=colorbar;
c.Label.String='u [pixels]';
plot([50;(50+(175/5))],[165;165],'-k','LineWidth',2)
text(50,175,'100 \mum','HorizontalAlignment','left')
title('u Discontinuity')

nexttile(3) %repeated from above
hold on
axis([1 colZero 1 rowZero])
c=colorbar;
c.Label.String='strain [-]';
plot([50;(50+(175/5))],[165;165],'-k','LineWidth',2)
text(50,175,'100 \mum','HorizontalAlignment','left')
title('exx')

nexttile(4) %repeated from above
hold on
axis([1 colZero 1 rowZero])
c=colorbar;
c.Label.String='u [pixels]';
plot([50;(50+(175/5))],[165;165],'-k','LineWidth',2)
text(50,175,'100 \mum','HorizontalAlignment','left')
title('u')

saveas(gcf,'2x2 strain map with discontinuities.tif') %save figure
```

ID discontinuities and compress into single line

```matlab
figure(2) %make all figures needed
figure(3)
figure(4)
figure(5)
figure(6)
figure(7)
figure(8)
figure(9)
figure(10)
figure(11)
figure(12)
xlabel('x position (pixels)')
ylabel('y position (pixels)')
hold on
set(gca,'ydir','reverse') %reverse y-axis to align with HRDIC images

for i=1:N %loop through all images
    sigmaTemp=C(i).sigma; %extract sigma
    uTemp=C(i).u; %extract u
    vTemp=C(i).v; %extract v

    sigmaWrite=zeros(rowZero,colZero); %presize all all matrices for outputs
    uWrite=zeros(rowZero,colZero);
    uWriteDiscSurround=zeros(rowZero,colZero);
    vWrite=zeros(rowZero,colZero);
    vWriteDiscSurround=zeros(rowZero,colZero);
    TotalWriteDiscSurround=zeros(rowZero,colZero);
    TotalWriteDisc=zeros(rowZero,colZero);

    ExtenseWriteDisc=zeros(rowZero,colZero);
    TotalWriteDiscMicron=zeros(rowZero,colZero);

    exxWrite=zeros(rowZero,colZero);
    eyyWrite=zeros(rowZero,colZero);
    exyWrite=zeros(rowZero,colZero);

    exxWriteDiscSurround=zeros(rowZero,colZero);
    eyyWriteDiscSurround=zeros(rowZero,colZero);
    exyWriteDiscSurround=zeros(rowZero,colZero);

    exxWriteDiscCompress=zeros(rowZero,colZero);
    for j=1:colZero %loop through all columns
        k=1; %set row index to 1
        while k<=rowZero %while loop to scan down each column, row by row
            sigmaSingle=sigmaTemp(k,j); %extract sigma at k,j index
            if sigmaSingle==-1 %if discontinuous enter extraction
                Disc=k; %begin tracking indexes within single discontinuity
                DiscOneAbove=k-1; %save index of point above discontinuity
                while sigmaSingle==-1 %loop until end of discontinuity is found
                    k=k+1; %increase row index by 1
```

70

```matlab
                    if k>rowZero %if possible index is exceeded, break out of while loop
                        break
                    end
                    sigmaSingle=sigmaTemp(k,j); %save next sigma value in index sequence
                    if sigmaSingle==-1 %add next index to total discontinuity tracker if still
within discontinuity
                        Disc(end+1)=k;
                    end
                end
                DiscOneBelow=k; %first point after end of discontinuity found and saved
                if DiscOneAbove==0 %Fix index error
                    DiscOneAbove=1;
                end
                if DiscOneBelow>=rowZero %Fix index error
                    DiscOneBelow=rowZero;
                end
                DiscCenter=mean(Disc); %average of discontinuity index to find center
                if floor(DiscCenter)~=DiscCenter %if index not integer, use random number
generator to determine to round up or down
                    prob=rand();
                    prob=round(prob);
                    if prob==1
                        DiscCenter=ceil(DiscCenter);
                    else
                        DiscCenter=floor(DiscCenter);
                    end
                end
                sigmaWrite(DiscCenter,j)=255; %write 255 to all discontinuity centers
                uWrite(DiscCenter,j)=uTemp(DiscCenter,j); %write u to all discontinuity centers
                uWriteDiscSurround(DiscOneBelow,j)=uTemp(DiscOneBelow,j); %write u and v for
points above and below discontinuities
                uWriteDiscSurround(DiscOneAbove,j)=uTemp(DiscOneAbove,j);
                vWriteDiscSurround(DiscOneBelow,j)=vTemp(DiscOneBelow,j);
                vWriteDiscSurround(DiscOneAbove,j)=vTemp(DiscOneAbove,j);

TotalWriteDiscSurround(DiscOneBelow,j)=sqrt((uTemp(DiscOneBelow,j)^2)+(vTemp(DiscOneBelow,j)^2));
%calculate displacement of points above and below discontinuities

TotalWriteDiscSurround(DiscOneAbove,j)=sqrt((uTemp(DiscOneAbove,j)^2)+(vTemp(DiscOneAbove,j)^2));
                TotalWriteDisc(DiscCenter,j)=abs(TotalWriteDiscSurround(DiscOneBelow,j)-
TotalWriteDiscSurround(DiscOneAbove,j)); %find difference, assumes opposite directions for the 2
points
                if abs(TotalWriteDisc(DiscCenter,j))>2.5 %filter out noise, number is adjustable
                    TotalWriteDisc(DiscCenter,j)=0;
                end

                ExtenseWriteDisc(DiscCenter,j)=TotalWriteDisc(DiscCenter,j)/(5*abs(DiscOneBelow-
DiscOneAbove)); %convert indexes to pixels based on step size and calculate extensometers
                TotalWriteDiscMicron(DiscCenter,j)=TotalWriteDisc(DiscCenter,j)*5*DistPerPixel;
%calculate total discontinuity between points in microns


exxWrite(DiscCenter,j)=(uTemp(DiscCenter,j)/(colZero*5))+(((uTemp(DiscCenter,j)/(colZero*5))^2+((
vTemp(DiscCenter,j)/(colZero*5))^2))/2); %lagrangian strain calculations, need to include other
```

```
indexes to match Vic-2D DIC output

eyyWrite(DiscCenter,j)=(vTemp(DiscCenter,j)/(rowZero*5))+(((uTemp(DiscCenter,j)/(rowZero*5))^2+((
vTemp(DiscCenter,j)/(rowZero*5))^2))/2);

exyWrite(DiscCenter,j)=((uTemp(DiscCenter,j)/(rowZero*5))+(vTemp(DiscCenter,j)/(colZero*5))+((uTe
mp(DiscCenter,j)/(colZero*5))+(uTemp(DiscCenter,j)/(rowZero*5)))+((vTemp(DiscCenter,j)/(colZero*5
))+(vTemp(DiscCenter,j)/(rowZero*5))))/2;

exxWriteDiscSurround(DiscOneBelow,j)=(uTemp(DiscOneBelow,j)/(colZero*5))+(((uTemp(DiscOneBelow,j)
/(colZero*5))^2+((vTemp(DiscOneBelow,j)/(colZero*5))^2))/2);

exxWriteDiscSurround(DiscOneAbove,j)=(uTemp(DiscOneAbove,j)/(colZero*5))+(((uTemp(DiscOneAbove,j)
/(colZero*5))^2+((vTemp(DiscOneAbove,j)/(colZero*5))^2))/2);
                exxWriteDiscCompress(DiscCenter,j)=exxWriteDiscSurround(DiscOneAbove,j)-
exxWriteDiscSurround(DiscOneBelow,j);
            else
                k=k+1; %increase row index if no discontinuity detected
            end
        end
    end
    figure(2) %plot to premade figures
    imagesc(sigmaWrite)

    figure(3)
    imagesc(exxWrite)

    figure(4)
    imagesc(eyyWrite)

    figure(5)
    imagesc(exyWrite)

    figure(6)
    imagesc(uWriteDiscSurround)

    figure(7)
    imagesc(exxWriteDiscCompress)

    figure(8)
    imagesc(vWriteDiscSurround)

    figure(9)
    imagesc(TotalWriteDiscSurround)

    figure(10)
    imagesc(TotalWriteDisc)

    figure(11)
    imagesc(ExtenseWriteDisc)

    figure(12)
    imagesc(TotalWriteDiscMicron)
```

```matlab
end


figure(2)
hold on
axis([1 colZero 1 rowZero]) %set axis
plot([10;(10+(175/5))],[170;170],'-k','LineWidth',2) %plot scale bar
text(50,180,'100 \mum','HorizontalAlignment','left') %plot scale bar text
c=colorbar;
c.Label.String='Sigma [pixels]'; %plot colorbar with label
title('sigma') %title
saveas(gcf,'sigma.tif') %save figure


figure(3) %repeated from above
hold on
axis([1 colZero 1 rowZero])
plot([10;(10+(175/5))],[170;170],'-k','LineWidth',2)
text(10,180,'100 \mum','HorizontalAlignment','left')
c=colorbar;
c.Label.String='Strain [-]';
title('exx')
saveas(gcf,'exx.tif')


figure(4) %repeated from above
hold on
axis([1 colZero 1 rowZero])
plot([10;(10+(175/5))],[170;170],'-k','LineWidth',2)
text(10,180,'100 \mum','HorizontalAlignment','left')
c=colorbar;
c.Label.String='Strain [-]';
title('eyy')
saveas(gcf,'eyy.tif')


figure(5) %repeated from above
hold on
axis([1 colZero 1 rowZero])
plot([10;(10+(175/5))],[170;170],'-k','LineWidth',2)
text(10,180,'100 \mum','HorizontalAlignment','left')
c=colorbar;
c.Label.String='Strain [-]';
title('exy')
saveas(gcf,'exy.tif')


figure(6) %repeated from above
hold on
axis([1 colZero 1 rowZero])
plot([10;(10+(175/5))],[170;170],'-k','LineWidth',2)
text(10,180,'100 \mum','HorizontalAlignment','left')
c=colorbar;
c.Label.String='u [pixels]';
```

```matlab
title('u of area around disc.')
saveas(gcf,'u of disconinuity surroundings.tif')


figure(7) %repeated from above
hold on
axis([1 colZero 1 rowZero])
plot([10;(10+(175/5))],[170;170],'-k','LineWidth',2)
text(10,180,'100 \mum','HorizontalAlignment','left')
c=colorbar;
c.Label.String='Strain [-]';
title('exx discontinuity compressed')
saveas(gcf,'Difference between exx around discontinuity.tif')

figure(8) %repeated from above
hold on
axis([1 colZero 1 rowZero])
plot([10;(10+(175/5))],[170;170],'-k','LineWidth',2)
text(10,180,'100 \mum','HorizontalAlignment','left')
c=colorbar;
c.Label.String='v [pixels]';
title('v of area around disc.')
saveas(gcf,'v of discontinuity surroundings.tif')

figure(9) %repeated from above
hold on
axis([1 colZero 1 rowZero])
plot([10;(10+(175/5))],[170;170],'-k','LineWidth',2)
text(10,180,'100 \mum','HorizontalAlignment','left')
c=colorbar;
c.Label.String='Displacement [pixels]';
title('Displacement of area around discontinuity')
saveas(gcf,'Displacement of discontinuity surroundings.tif')

figure(10) %repeated from above
hold on
axis([1 colZero 1 rowZero])
plot([10;(10+(175/5))],[170;170],'-k','LineWidth',2)
text(10,180,'100 \mum','HorizontalAlignment','left')
c=colorbar;
c.Label.String='Displacement [pixels]';
title('Total Discontinuity')
saveas(gcf,'Total discontinuity.tif')

figure(11) %repeated from above
hold on
axis([1 colZero 1 rowZero])
plot([10;(10+(175/5))],[170;170],'-k','LineWidth',2)
text(10,180,'100 \mum','HorizontalAlignment','left')
c=colorbar;
c.Label.String='\DeltaL/L_0';
title('Extensometer')
saveas(gcf,'Extensometer.tif')
```

```
figure(12) %repeated from above
hold on
axis([1 colZero 1 rowZero])
plot([10;(10+(175/5))],[170;170],'-k','LineWidth',2)
text(10,180,'100 \mum','HorizontalAlignment','left')
c=colorbar;
c.Label.String='Displacement [\mum]';
title('Displacement along discontinuities')
saveas(gcf,'MicronDisc.tif')
```

Published with MATLAB® R2020b